EES Batteries

Accepted Manuscript

This article can be cited before page numbers have been issued, to do this please use: X. Tang, F. Xie, X. Rong, Y. Lu, L. Chen and Y. Hu, *EES Batteries*, 2025, DOI: 10.1039/D5EB00064E.

View Article Online
DOI: 10.1039/D5EB00064E

Halide-based Solid Electrolytes: Opportunities and Challenges in Synergistic Development of All-Solid-State Li/Na Batteries

Xiaohan Tang,[a] Fei Xie,[a*] Yaxiang Lu,[a,b,c] Xiaohui Rong,[a,b,d] Liquan Chen,[a, b, c, d] and Yong-Sheng Hu[a, b, c, d*]

[a] Key Laboratory for Renewable Energy, Beijing Key Laboratory for New Energy Materials and Devices, Beijing National Laboratory for Condensed Matter Physics, Institute of Physics, Chinese Academy of Sciences, Beijing, 100190, China

[b] College of Materials Science and Optoelectronics Technology, University of Chinese Academy of Sciences, Beijing, 100049, China

[c] Huairou Division, Institute of Physics, Chinese Academy of Sciences, Beijing 101400, China

[d] Yangtze River Delta Physics Research Center Co. Ltd., Liyang, 213300, China

Email: fxie@iphy.ac.cn; yshu@iphy.ac.cn

View Article Online
DOI: 10.1039/D5EB00064E

Abstract

In the ever-evolving wave of energy storage technologies, all-solid-state batteries (ASSBs) have garnered significant attention due to their high energy density, long cycle life and intrinsic safety, being regarded as a necessary step of next-generation batteries. Halide-based solid electrolytes have emerged as promising candidates for next-generation ASSBs owing to their superior oxidative stability and tunable high ionic conductivity. This review aims to provide a comprehensive overview of the latest advances and state-of-the-art research progress in Li- and Na-based halide electrolytes. The common synthesis strategies, various categories of halide-based electrolytes, and their ion transport mechanisms are introduced in detail. Furthermore, various modification strategies for improving ionic conductivity, air stability and electrochemical stability are also discussed. Finally, we also offer insights into the current challenges and future perspectives of halide-based electrolytes. We anticipate that this review can serve as a guide for the design and understanding of halide-based electrolytes and promote their further advancement in the application of ASSBs toward energy storage.

Broader text: Against the background of rapidly advancing global energy storage technologies, all-solid-state batteries (ASSBs) have increasingly attracted widespread attention from both researchers and industry due to their unique advantages. As a crucial component of ASSBs, the properties of solid electrolytes play a significant role in their overall development. Halide-based electrolytes, an emerging class of solid electrolytes materials, have shown great potential in next-generation ASSBs research because of their excellent ionic conductivity and strong compatibility with oxide cathodes. In this review, we provide a comprehensive overview of the development trends and technical challenges of Li-based and Na-based halide electrolytes. We place particular emphasis on common synthesis methods, various structural types, and their ion transport behaviors. This review also systematically summarizes a series of modification techniques aimed at enhancing the ionic conductivity, air stability, and

View Article Online
DOI: 10.1039/D5EB00064E

electrochemical stability of halide-based electrolytes. Finally, the article analyzes the main challenges of halide-based electrolytes faced in practical applications and proposes potential strategies for future development to promote their widespread use in ASSBs.

1. Introduction

The rapid evolution of renewable energy systems and electrified transportation has intensified the demand for advanced energy storage technologies that combine high energy density, intrinsic safety, and long-term stability. Conventional Li-ion batteries (LIBs), despite their commercial success, face inherent limitations due to their reliance on flammable organic liquid electrolytes.[1, 2] These electrolytes pose significant safety hazards, including leakage, thermal runaway, and combustion or even explosion under mechanical or thermal stress, which are exacerbated in high-energy applications such as electric vehicles (EVs) and grid-scale energy storage systems.[3-6] Furthermore, the scarcity and uneven global distribution of Li and Co resources, coupled with the fluctuating costs, have spurred interest in alternative battery technologies, particularly Na-ion batteries (NIBs), which leverage Na's natural abundance and cost-effectiveness.[7-11] However, NIBs also inherit the safety drawbacks from the liquid electrolytes, hindering their scalability for large deployments. All-solid-state batteries (ASSBs), which replace liquid electrolytes with solid-state counterparts, have emerged as a transformative solution to these challenges. By eliminating the flammable components, ASSBs are able to inherently mitigate fire and explosion hazards while enabling the use of high-capacity metallic anodes (e.g., Li or Na), thereby significantly boosting the energy density.[8, 12-14] In addition, without the liquid electrolyte with fluidity, the bipolar configurations are feasible with SEs to increase the voltage and energy density of the cells, and continuous interfacial side reactions can be effectively impeded during the charge/discharge processes, so that the cyclic lifespan could be prolonged in ASSBs.[15]

Solid electrolytes (SEs), as a critical component of ASSBs, decisively influence the battery performance. To achieve satisfactory electrochemical performance in

View Article Online
DOI: 10.1039/D5EB00064E

ASSBs, the prerequisite is the development of solid electrolytes with high ionic conductivity, high electronic resistivity, excellent chemical and electrochemical stability, excellent machinability, and favorable interfacial compatibility.[16, 17] As early as the 1980s, Na-β-Al_2O_3 were used as electrolytes in high-temperature Na-S batteries and Na-Fe/$NiCl_2$ batteries.[18] However, these batteries could only operate at temperatures >300°C, which increased the operational costs and safety risks. Through years of efforts, various types of SEs have been developed to meet the requirements for ASSBs operating at lower temperatures (<80°C). Nevertheless, they still face some shortcomings such as relatively low room-temperature ionic conductivity, narrow electrochemical stability windows, and poor electrode/electrolyte interfacial compatibility. Currently, the most prominent Na-ion solid electrolytes include oxide-, halide-, sulfide-, borohydride-, and polymer-based electrolytes (**Figure 1a**).[19-21] Oxide-based electrolytes (e.g., Na-β-Al_2O_3 and NASICON) can achieve room-temperature ionic conductivities >10^{-3} S cm^{-1}. However, they require extremely high sintering temperatures (>1000 °C) to reduce grain boundary resistance and exhibit poor interfacial contact with electrodes due to their high mechanical rigidity.[22, 23] Sulfide-based electrolytes possess relatively higher room-temperature ionic conductivities over 10^{-2} S cm^{-1} and soft mechanical properties that enable cold-press densification.[24, 25] Nevertheless, their inherently narrow electrochemical stability windows restrict the choices of cathode materials. They are also unstable against Na metal anodes and sensitive to moisture, which can cause the toxic H_2S released. Borohydride-based electrolytes, offering high ionic conductivity and superior reduction stability, are hindered by costly raw materials and complex synthesis.[26-28] Polymer-based electrolytes are typically flexible, enabling good interfacial contact and electrode compatibility, but they face challenges such as low room-temperature ionic conductivity and narrow electrochemical windows.[29, 30]

Halide-based electrolytes have recently garnered significant attention due to the inherent chemical properties of halide anions, which enable high ionic conductivity, high oxidative stability (>4 V vs. Li^+/Li or >4 V vs. Na^+/Na), and good deformability.[31, 32] In fact, research on the conductivity of LiX and ternary Li-X-M halides dates back

to as early as 1930s.[33] However, their low ionic conductivity (<10^{-5} S cm^{-1}) initially limited interest in halide-based electrolytes, causing research stagnation until 2018. In that year, Asano et al. synthesized Li_3YCl_6 and Li_3YBr_6 via ball milling and annealing, achieving room-temperature ionic conductivities of 0.51×10^{-3} S cm^{-1} and 1.7×10^{-3} S cm^{-1}, respectively.[34] Since then, a series of novel halide superionic conductors have emerged, including water-mediated synthesis of Li_3InCl_6[35], ball-milled and sintered Li_2ZrCl_6[36] and Li-Ta-O-Cl[37, 38], and viscoelastic-like $LiAlCl_{2.5}O_{0.75}$[39]. The best-reported room-temperature ionic conductivity reaches 10^{-2} S cm^{-1}, rivaling state-of-the-art sulfide electrolytes and liquid electrolytes.[38] Additionally, halides exhibit high voltage stability (>4 V vs. Li^+/Li or >4 V vs. Na^+/Na). However, most studied halide-based electrolytes are Li-ion systems, with only a few Na-ion examples such as Na_2ZrCl_6[40], $NaAlCl_{2.5}O_{0.75}$[39], $NaTaCl_6$[41], $Na_{3-x}M_{1-x}Zr_xCl_6$ (M=Y, Er)[42, 43], and $NaMCl_4O$ (M=Ta, Nb)[44], all of which underperform compared to their Li-based analogs. Despite their promising ionic conductivity and oxidative stability, practical applications of halide-based electrolytes remain hindered by challenges such as high raw material costs, complex synthesis steps, air sensitivity, and instability at the anode interface.

Current studies on halide-based electrolytes remains in its early stages, with limited understanding of their ion transport mechanisms, interfacial compatibility with electrodes, and thermal/mechanical failure mechanisms. Additionally, there is a significant room for improvement in ionic conductivity. In this review, we provide a comprehensive summary of the synthesis methods, categories, ion transport mechanisms, and chemical/electrochemical stabilities for Li/Na-based halide electrolytes. The outline structural design and modification strategies to enhance their performance were also discussed. Finally, we present insights into the current challenges and suggest future research perspectives for halide-based electrolytes.

View Article Online
DOI: 10.1039/D5EB00064E

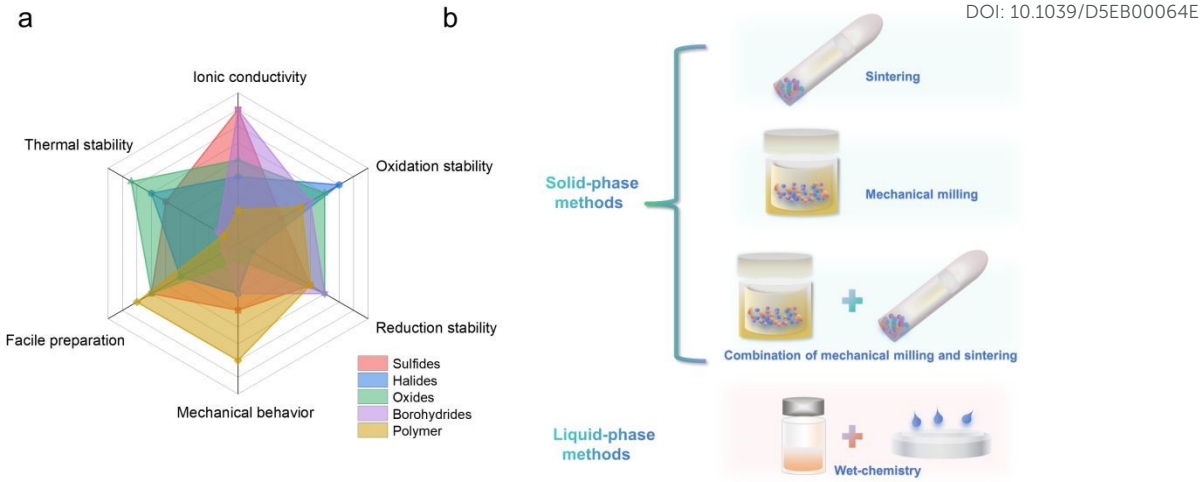

Figure 1. (a) The radar chart compares the performance of key parameters of various solid-state electrolytes. (b) The schematic diagram of the solid-phase and liquid-phase methods of halide-based electrolytes.

2. Synthesis strategies

Synthesis strategies play a critical role in determining the properties of SE materials. Different processing routes and atmospheric conditions can significantly influence their structures, crystallinity, and ionic conductivity. Due to the air-sensitive and hygroscopic nature of the raw halide compounds, most synthesis procedures must be conducted under inert atmospheres (e.g., gloveboxes) or below the dew point to prevent moisture-induced degradation. Current synthesis methods for halide-based electrolytes primarily include solid-phase methods (mainly involve solid-phase sintering and mechanochemical protocol) and liquid-phase methods (water-mediated synthesis and ammonium-assisted synthesis), as shown in **Figure 1b**.

Solid-phase synthesis is the most widely used method for preparing halide-based electrolytes. Early approaches involved sealing anhydrous raw materials into quartz tubes under vacuum or inert atmospheres for solid-state sintering. However, this method requires prolonged annealing times due to sluggish reaction kinetics between solid compounds, although it can enhance the phase stability and crystallinity.[45, 46] Additionally, some binary halide mixtures exhibit low eutectic temperatures, enabling molten-state reactions during sintering, which can further shortening the processing durations.[47, 48]

Mechanochemical strategies represented by the ball milling offers an alternative

View Article Online
DOI: 10.1039/D5EB00064E

solid-phase route that can improve the homogeneity of the raw materials during the synthesis and reduce the reaction time. The mechanical energy generated during the milling provides activation energy for the interactions among the precursors, yielding new materials distinct from the starting components. Unlike traditional sintering, high-energy ball milling produces disordered or locally distorted crystal structures and amorphous phases.[49, 50] These structural defects and amorphous domains can often enhance the ionic conductivity of the resulting halide-based electrolytes, in particular for the Na-based systems due to the larger ionic radius of Na^+, so that the ionic transport will be highly impeded by some unsatisfied crystalline configurations and narrow bottlenecks. Notably, the high-energy ball milling was also reported to combine with subsequent annealing, where the ball milling can be used to improve the uniformity of raw material mixing and thus reduce the time of solid-phase annealing reaction. For example, the annealing times were reduced to 1 h by introducing ball milling in advance to prepare for Li_3ErCl_6.[51]

Liquid-phase methods enable faster reaction kinetics, precise particle size control, and scalability for mass production. In 2019, Sun's group pioneered the aqueous synthesis of Li_3InCl_6 by solving LiCl and $InCl_3$ in water to form a hydrated intermediate ($Li_3InCl_6 \cdot xH_2O$), followed by vacuum heating.[35] The resulting Li_3InCl_6 achieved an ionic conductivity of 2.04×10^{-3} S cm^{-1}, surpassing the values of the one made from solid-phase methods. However, such this aqueous approach remains limitation to specific systems because most halide-based electrolytes cannot reversibly transform between hydrated and anhydrous states.

Another liquid-phase routes involve organic solvents, but these are often complex and generate more pollutants. For example, Wang et al. developed an ammonium-assisted wet chemical method, introducing NH_4Cl to form intermediate $(NH_4)_3[MCl_6]$ complexes, and subsequent heat treatment produced halide electrolytes like Li_3YCl_6.[52] This method can successfully suppress the formation of M-O-Cl impurities during the pyrolysis process, and also can be extended to some halide electrolytes with high-conductivity such as Li_3ScCl_6 (1.25 mS cm^{-1}), Li_3ErCl_6 (0.41 mS cm^{-1}), and Li_3YBr_6 (1.08 mS cm^{-1}). Despite its versatility, this method releases corrosive gases (e.g., HCl,

View Article Online
DOI: 10.1039/D5EB00064E

HBr) during ammonium salt decomposition, posing challenges for equipment durability and cost efficiency in large-scale production.

Currently, the synthesis of halide-based electrolytes is still primarily based on solid-phase methods, in particular the mechanochemical strategy, while the reports on liquid-phase methods remaining relatively scarce. The selection of precursors and process parameters (such as ball-milling reaction time, ball-to-material ratio, the temperature, duration and atmosphere of sintering) play a decisive role in the structure of halide-based electrolytes. For large-scale utilization of the halide-based electrolytes, it is still urgent to develop the synthesis methods that are low-cost, time-efficient, and easy to operate.

3. Structural type and diffusion mechanisms of halide-based electrolytes

Halide-based electrolytes are typically described by the chemical formula Li/Na_aMX_b (M= metal element, X=F, Cl, Br, I). As M or X changes, it can lead to variations in the arrangement of anions and the occupancy of cation sites, thereby affecting the structure, ion transport mechanisms, and ionic conductivity of the halide-based electrolytes. In this manuscript, we classify the halide-based electrolytes into three types (**Figure 2a** and **Table 1**): the anionic frameworks (exemplified by the cubic close-packed sublattice in Li_3InCl_6), the cationic frameworks (UCl_3-type), and amorphous.

3.1 Anionic Frameworks (Li/Na-M-X, X=F, Cl, Br, I)

In the crystal structure of anion framework-type halides electrolytes, the halide anions form a three-dimensional framework by sharing corners or edges, with metal cations (such as Y^{3+}, In^{3+}, and Sc^{3+}) occupying octahedral or tetrahedral sites, while Li^+/Na^+ are distributed within the framework's interstices. In Li/Na-M-X compounds, the anions typically form a sublattice composed of cubic close-packed (ccp) structure with an ABCABC stacking and hexagonal close-packed (hcp) structure with an ABAB stacking (**Figure 2b**).[53] However, the choice of metal cations, particularly their ionic

radii, plays a decisive role in determining the crystal structure. Each close-packed structure can be further subdivided into crystal structures with different space groups, such as monoclinic (*C2/m*, $P2_1/n$) and cubic spinel ($Fd\bar{3}m$) structures for the ccp anion sublattice, as well as trigonal ($P\bar{3}m1$) and orthorhombic (*Pnma*) structures for the hcp anion sublattice (**Figure 2c**). Moreover, in addition to these close-packed crystal configurations, other common structures were formed for specific compounds including olivine-type (high-temperature Li_2ZnCl_4, Na_2ZnCl_4, and Na_2CoCl_4),[54, 55] Suzuki-type (Li_6MCl_8, M= V, Fe, Co, Ni and Li_6MnBr_8),[56, 57] and Sr_2PbO_4-type structures (Na_2MgCl_4, Na_2MnCl_4, and Na_2CdCl_4),[58] as shown in **Figure 2c**.

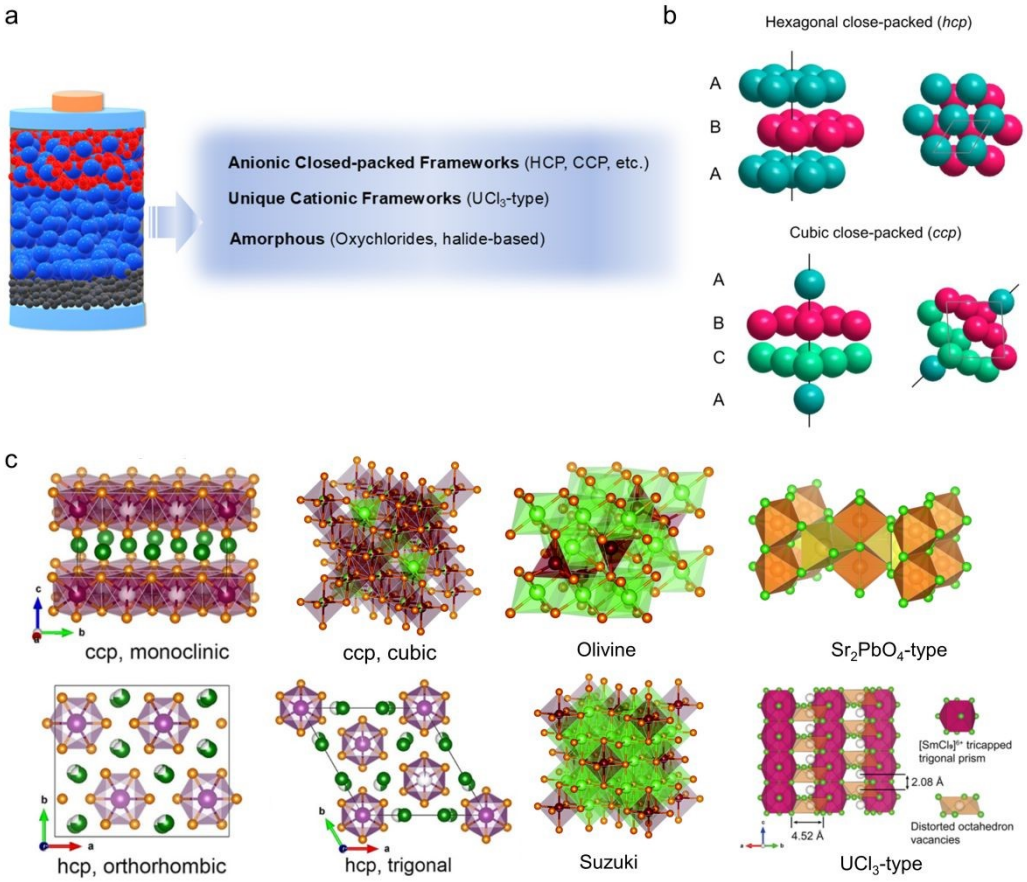

Figure 2. (a) Classify the existing halide-based electrolytes into three categories based on structural differences. (b) The cubic close-packed (ccp) structure and hexagonal close-packed (hcp) structure.[53] (c) The crystal structure diagrams of monoclinic, cubic, orthorhombic, trigonal, Suzuki, olivine, Sr_2PbO_4- and UCl_3-type.[32, 55, 59, 60]

Monoclinic halide electrolytes with ccp anion sublattice in Li-M-X electrolytes generally possess higher ionic conductivity and lower migration barrier. Currently, the octahedral sites of monoclinic Li-M-X electrolytes are usually occupied by M^{3+} cations

with an ionic radius less than 100 pm, mainly represented by Li_3InCl_6,[35] Li_3ScCl_6[61] and Li_3MBr_6 (M = In, Y, Sm-Lu),[45] etc. Moreover, some researchers have computationally predicted that Li_3MI_6 (M = Sc, Y, La, etc.) could possess superionic conductor characteristics.[62] However, in fact only Li_3ErI_6 with an ionic conductivity of 0.65×10^{-3} S cm^{-1} was successfully synthesized so far.[63] This is primarily due to the higher polarizability of I compared to Cl, which results in a softer lattice framework that is more conducive to Li^+ transport. In addition, Sun's and Wagemaker's groups both proposed the cation polarization factor and ionic potential, respectively, to guide the synthesis of monoclinic structures with high ionic conductivity (**Figure 3a-b**).[53, 64] Nevertheless, there is still some exceptions such as the monoclinic Na_3YCl_6 with $P2_1/n$ space group, which can be produced by slow cooling, but the ionic conductivity is extremely low (10^{-6} S cm^{-1} at 500 K).[65]

Spinel-based halide electrolytes are also constructed from ccp, but they exhibit relatively low ionic conductivity at room temperature. As early as the 1980s to 1990s, Ryoji Kanno and H. D. Lutz, et al. systematically investigated spinels based on divalent metal cations (such as the first-row transition metals, Mg, Pb, etc.), where Li^+ have two different occupation sites in the structure.[66, 67] In the inverse spinel structure Li_2MCl_4 (M = Mg, Mn, Cd), half of the Li occupy the corner-sharing tetrahedral sites, while the remaining of Li occupy the octahedral sites together with the divalent metal cations.[68] Due to the favorable phase transition at high temperature, the high-temperature phase can achieve an ionic conductivity of up to 10^{-2} S cm^{-1}. In the spinel structure of Li_2ZnCl_4, Li^+ are all resided in octahedral sites, while Zn^{2+} occupy the tetrahedral sites.[54] However, this ion distribution will hinder the Li^+ transportation, resulting in lower ionic conductivity. Moreover, Nazar's group synthesized a disordered spinel structure of $Li_2Sc_{2/3}Cl_4$ with a high ionic conductivity of 1.5×10^{-3} S cm^{-1}.[69] Compared with Li_2MgCl_4, the structure has four different sites of Li, and the disordered distribution of Li^+ in tetrahedral and octahedral sites also forms a three-dimensional ion diffusion channel composed of face-sharing octahedra and tetrahedra, thereby achieving high ionic conductivity (**Figure 3c**).

View Article Online
DOI: 10.1039/D5EB00064E

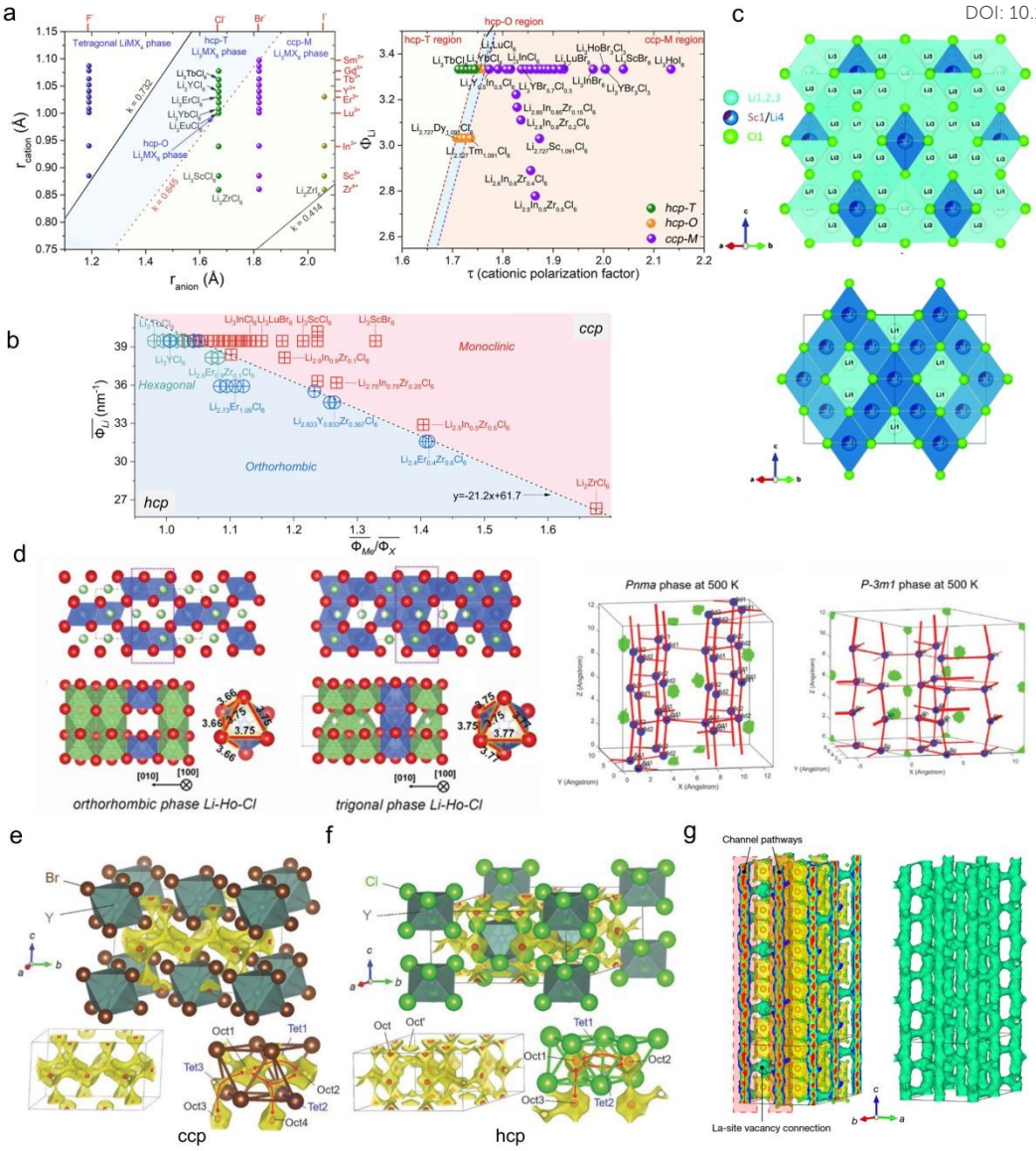

Figure 3. The phase map showing representative halid-based electrolytes as a fuction of (a) cation polarization factor[64] and (b) ionic potential[53] to guide the synthesis of monoclinic structures with high ionic conductivity. (c) The disordered spinel structure $Li_2Sc_{2/3}Cl_4$.[69] (d) The structure of orthorhombic and trigonal structures of Li_3HoCl_6, and the ionic jumps between different Li sites.[70] Crystal structure and Li^+ migration path of (e) Li_3YCl_6 and (f) Li_3YBr_6.[34] (g) The 3D Li^+ migration pathways of UCl_3-type $Li_{0.388}Ta_{0.238}La_{0.475}Cl_3$.[71]

The hcp close-packed structure of halide electrolytes is mainly composed of trigonal ($P\bar{3}m1$) and orthorhombic (*Pnma*) phases. The metal cations in the trigonal phase has a larger ionic radius than the orthorhombic phase, but the ionic conductivity of the orthorhombic phase is usually one order of magnitude higher than that of the trigonal phase. Representatives electrolytes of the trigonal phase with the $P\bar{3}m1$ space group include Li_3MCl_6 (M = Y, Tb–Tm),[34, 51, 72, 73] α-Li_2ZrCl_6,[36] Na_2ZrCl_6,[40] and

View Article Online
DOI: 10.1039/D5EB00064E

Na_3InCl_6,[74] which have low room-temperature ionic conductivities, ranging from 10^{-5} to 10^{-4} S cm^{-1}. Li_3YCl_6 synthesized by Asano as a typical example of the trigonal phase has been widely studied.[34] In this structure, Y^{3+}, Li^+, and vacancies occupy the octahedral sites in a molar ratio of 1:3:2, and the existence of vacancies is the key to achieving an ionic conductivity of 10^{-4} S cm^{-1}. Furthermore, Mo's group calculated the theoretical room-temperature ionic conductivity of Li_3YCl_6 to be 1.4×10^{-2} S cm^{-1} through AIMD.[75] However, the experimental value is two orders of magnitude lower, primarily because the similar ionic radius of Li^+ and Y^{3+}, which leads to their disordered distribution at the octahedral sites to form antioccupied defects, thus causing the block of Li^+'s transport. The impurities and grain boundaries during synthesis also affect the conductivity. Based on theoretical calculations, Sokseiha Muy and colleagues predicted and successfully synthesized Li_3ErCl_6 via ball-milling, which is isostructural with Li_3YCl_6, but the ionic conductivity would be decreased after sintering from 0.3×10^{-3} S cm^{-1} to 0.05×10^{-3} S cm^{-1}.[51] Na_2ZrCl_6 synthesized via ball milling shows an ionic conductivity of 1.8×10^{-5} S cm^{-1}, which also decreases after heating treatment since the crystallinity is enhanced.[40] The highly crystalline phase attributed to the strong bonding between Na and Cl in the lattice will decline the ionic conductivity. The orthorhombic structures with the *Pnma* space group include Li_3MCl_6 (M= Y, Ho-Lu) can deliver the room-temperature ionic conductivities ranging from 0.32 to 1.3×10^{-3} S cm^{-1}. Sun's group found that in the ternary chloride solid electrolytes $Li_{3-3x}M_{1+x}Cl_6$ ($-0.14<x\leq0.5$, M= Tb, Dy, Ho, Y, Er, Tm) is beneficial to the structure transformation from the trigonal to the orthorhombic phase and significantly enhances the ion conductivity as the x value increases (**Figure 3d**).[70] Among them, the ion conductivity of the orthorhombic phase $Li_{2.73}Ho_{1.09}Cl_6$ reaches as high as 1.3×10^{-3} S cm^{-1}, around four times higher than that of the trigonal phase. This improvement is attributed to the formation of the orthorhombic phase, which makes it easier for Li^+ transport along the c-axis.

Halide electrolytes exhibit different anion packing arrangements, which also lead to variations in Li^+ transport pathways and dynamics. In ccp anion sublattices, Li^+ typically occupy octahedral and tetrahedral sites, allowing migration along crystal

View Article Online
DOI: 10.1039/D5EB00064E

planes and interstitial sites through multiple directions. These interconnected pathways form a complex but highly efficient three-dimensional transport network, and the diffusion is isotropic, which facilitates rapid ion migration. Li^+ usually jump from one octahedral site, pass through a tetrahedral site, and finally reach an adjacent octahedral site, namely Oct1-[Tet1 or Tet2]-Oct2 and Oct1-Tet3-Oct3 (**Figure 3e**). In contrast, the diffusion of Li^+ in the hcp anion sublattice is anisotropic. In the ab plane, Li^+ mainly migrate via tetrahedral sites (Oct1-[Tet1 or Tet2]-Oct2), while along the c-axis, they diffuse through octahedral sites (Oct1-Oct3), as shown in **Figure 3f**.

3.2 Cationic Frameworks (UCl_3-Type)

The UCl_3-type superionic conductors have attracted significant attention due to their unique cationic framework and large ion transport channels. Their structure is based on the lattice of lanthanum chloride $LnCl_3$ (Ln= La, Ce, Sm, Nd, etc.), which is composed of nine-coordinated $[LnCl_9]^{6-}$ polyhedrons (**Figure 2c**). The Cl^- are arranged in a non-close-packed anion framework forming a larger one-dimensional diffusion channels. Owing to the large radius of Ln^{3+} (ranging from 124.7 pm to 135.6 pm) and the non-close-packed structure, the diffusion channels and coordination distortions are significantly larger than those in traditional close-packed structure of Li/Na-M-X. However, the existing one-dimensional channels in the lattice are easily affected by blocking effects, leading to the lower ion diffusivity. To address this, Yao and colleagues first introduced Ta^{5+} doping to create La vacancies and construct three-dimensional ion transport pathways (**Figure 3g**).[71] The synthesized $Li_{0.388}Ta_{0.238}La_{0.475}Cl_3$ achieved a high ionic conductivity of 3.02×10^{-3} S cm^{-1} at room temperature and exhibited excellent stability against metallic lithium anodes due to the low electronegativity of lanthanide elements. Additionally, Sun et al. reported a zeolite-like $SmCl_3$ framework structure.[60] The ionic conductivity of ball-milled (BM) electrolytes likes BM-$SmCl_3$-0.5LiCl and BM-$SmCl_3$-0.5Li_2ZrCl_6 exhibited 1.2×10^{-4} S cm^{-1} and 1.0×10^{-3} S cm^{-1}, respectively. In fact, as early as in 1994, Meyer reported Na-based UCl_3-type compounds $Na_{3x}M_{2-x}Cl_6$ (M = La-Sm) and NaM_2Cl_6 (M = Nd, Sm), although their ionic conductivity were much lower than 10^{-4} S cm^{-1}.[76] Recently, Xiang

et al. synthesized $Na_{0.7}La_{0.7}Zr_{0.3}Cl_4$ with ionic conductivity of 2.9×10^{-4} S cm^{-1}.[77] The moderate ionic conductivity was attributed to the doping of Zr^{4+} at the La^{3+} sites, which shortens the lengths of Zr-Cl and La-Cl bonds, expanding the Na^+ diffusion pathways and improving ionic conductivity. However, due to the anti-site defects between La and Na, a small fraction of La^{3+} in the one-dimensional diffusion pathways hinders the Na^+ transport and ultimately reduced the ionic conductivity. Furthermore, Sun's group developed a novel halide heterostructure by combining the high-coordination UCl_3-type framework ($Na_{0.75}M_{1.75}Cl_6$, M= La, Sm) with the Ta-based low-coordination amorphous halide electrolyte ($NaTaCl_6$).[78] The synthesized $0.62[Na_{0.75}Sm_{1.75}Cl_6]$-$0.38[NaTaCl_6]$ and $0.57[Na_{0.75}La_{1.75}Cl_6]$-$0.43[NaTaCl_6]$ exhibited high ionic conductivities of 2.7 mS cm^{-1} and 1.8 mS cm^{-1}, respectively. The amorphous regions are conducive to connecting discrete UCl_3-type particles, enabling long-range Na^+ diffusion and improved ionic conductivity. Currently, the development of UCl_3-type electrolytes remains limited, which have more promising opportunities for further research.

3.3 Amorphous halide electrolytes

Among halide-based electrolytes, Li-based materials are still predominantly crystalline and some amorphous electrolytes with high ionic conductivity have also emerged, whereas Na-based electrolytes are mainly in the amorphous state. Amorphous halide-based electrolytes offer many advantages such as abundant intrinsic defects, few grain boundaries, and large transport spaces. However, due to the lack of long-range order in the structure, it is currently difficult to clearly explore their accurate ion transport mechanisms, and the study in this area is still in the early stage. The main representatives of amorphous compounds include Li/$NaTaCl_6$,[41, 79] Li/$NaTaOCl_4$[37, 80] and clay-like systems such asc.[81] Yao et al. successfully synthesized amorphous Li–Ta/Nb–Cl-based and composite electrolytes with various lithium salts such as LiF, Li_2O, LiOH, and Li_2O_2 via ball milling.[79] The room-temperature ionic conductivity can reach up to 7×10^{-3} S cm^{-1}, which is mainly due to the inherent properties of the amorphous structure and the efficient Li^+ transport at the interfaces with LiCl particles. In the

amorphous matrix, an appropriate amount of LiCl can release mobile Li^+ to promote conduction, whereas an excess of LiCl may impede the process. Similarly, NaCl and $TaCl_5$ can also be used to synthesize amorphous $NaTaCl_6$ with high ionic conductivity (4×10^{-3} S cm^{-1}) through long-term ball milling.[41] This is mainly due to the weakening of Na–Cl interactions, while the high-energy ball milling deforms the $TaCl_6$ octahedron and forms a poly-$TaCl_6$ framework, which repels Na^+ from entering the amorphous matrix and promotes their rapid migration (**Figure 4a**). In addition, a new type of clay-like electrolyte materials xLiCl–GaF_3 with high ionic conductivity was reported with amorphous structures, which is attributed to $Ga(F,X)_n$ polyanions that weakening the Li–X interactions through charge aggregation and thereby, promoting the Li^+ transport (**Figure 4b**).[82, 83] However, only the Li–Ga–F–Cl and analogous Mg-Ga-F-Cl systems have successfully obtained as the clay-like lithium and magnesium conductors, respectively.[84] The formation principle of the clay-like properties and the corresponding clay-like electrolytes for Na-based batteries or based on other precursors in addition to GaF_3 still require further exploration.

Table 1. Types of the halide-based electrolytes

	Crystal structure	Packing style	Representative electrolyte
Anionic Frameworks	Monoclinic (*C2/m*, *P2₁/n*)	CCP	Li_3InCl_6, Li_3ScCl_6 ,Na_3YCl_6
	Cubic spinel ($Fd\bar{3}m$)	CCP	Li_2MCl_4 (M = Mg, Mn, Cd)
	Trigonal ($P\bar{3}$ *m1*)	HCP	Li_3MCl_6 (M = Y, Tb-Tm), Na_2ZrCl_6, Na_3InCl_6
	Orthorhombic (*Pnma*)	HCP	Li_3MCl_6 (M= Y, Ho-Lu)
	Olivine-type	-	high-temperature Li_2ZnCl_4, Na_2ZnCl_4, and Na_2CoCl_4
	Suzuki-type	-	Li_6MCl_8, M= V, Fe, Co, Ni and Li_6MnBr_8
	Sr_2PbO_4-type	-	Na_2MgCl_4, Na_2MnCl_4, and Na_2CdCl_4
Cationic Frameworks	UCl3-Type	non-close-packed	$Na_{3x}M_{2-x}Cl_6$ (M = La-Sm) and NaM_2Cl_6 (M = Nd, Sm)

Amorphous	-	-	Li/$NaTaOCl_4$, Li/$NaTaOCl_4$-$LiAlCl_{2.5}O_{0.75}$

4. Modification strategies of halide-based electrolytes towards higher ionic conductivity

Although halide-based electrolytes have achieved remarkable progress over the past few years, ionic conductivity is still a key factor hindering their widespread application in ASSBs. Currently, only a few halide-based electrolytes can reach an ionic conductivity over 10^{-3} S cm^{-1}. To promote their practical application in ASSBs, it is essential to explore and implement effective strategies to further enhance their ionic conductivity. The common strategies mainly involve substituting anions/cations with different radius or valences, amorphization, and increasing the configuration entropy, which can effectively regulate the sublattice structures, charge carriers, and defect concentrations of the halide-based electrolytes, thereby optimizing ion diffusion and improving the ionic conductivity.

View Article Online
DOI: 10.1039/D5EB00064E

4.1 Cation modification

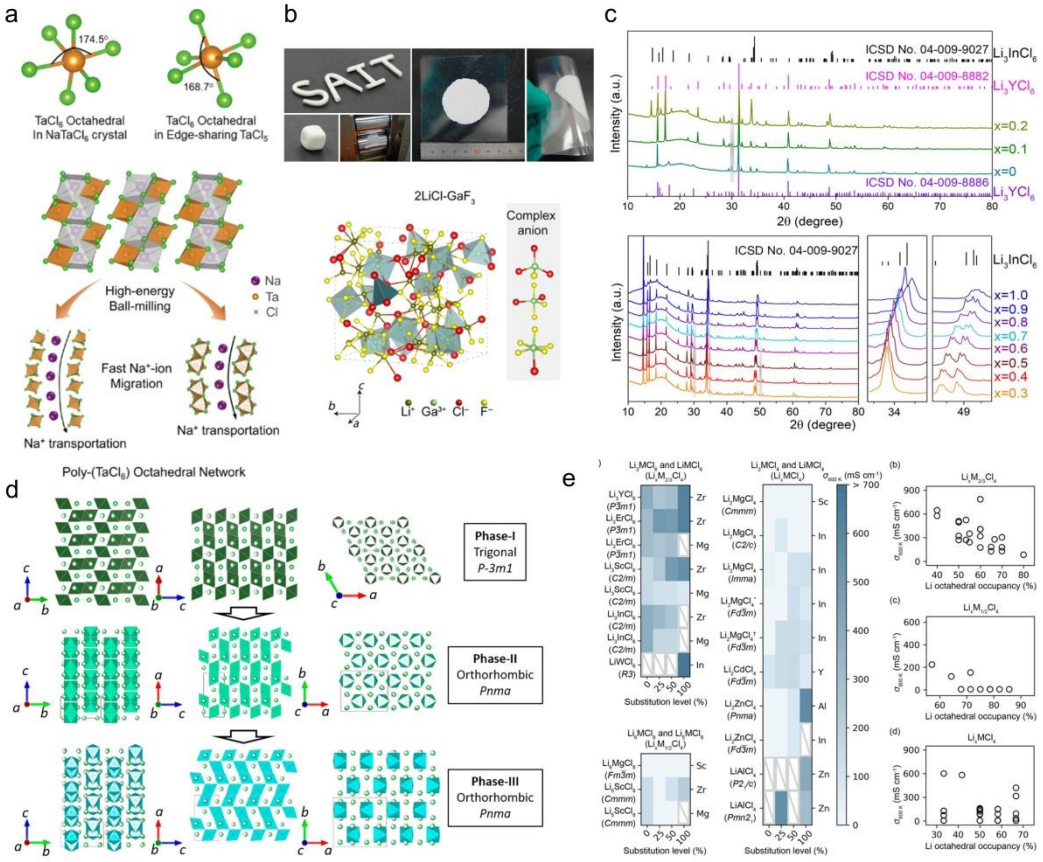

Figure 4. (a) The Na^+ conduction mechanism and local structural distortion in $NaTaCl_6$.[41] (b) The clay-like amorphous electrolyte xLiCl-GaF_3.[82, 83] (c) By partially substituting In^{3+}, $Li_3Y_{1-x}In_xCl_6$ can transition from cubic phase to trigonal phase.[59] (d) $Li_{3-x}M_{1-x}Zr_xCl_6$ (M=Y, Er) with different amount of Zr doping will result phase transition.[85] (e) Effecting on conductivity through tailoring the cation lattice and Li-content by high-throughput computational analysis.[86]

Cation modification is primarily achieved by introducing isovalent or aliovalent cations into the pristine frameworks. According to the differences in ionic radius and chemical bond characteristics among isovalent cations, isovalent substitution can alter the crystal structure and optimize the sublattice configuration to improve ion transport pathways and thereby increase the ionic conductivity. Ciucci and co-workers used density functional theory (DFT) to investigate the effects of metal cations with different ionic radii (M = Sr, Sc, La, Zr) on the partially substitution in Li_3YCl_6.[87] It was found that partial substitution of Y by a larger cation such as La can enlarge the diffusion channels and lower the activation energy. In addition, the ionic conductivity can be improved by changing the doping level of isovalent cations, which can induce crystal

View Article Online
DOI: 10.1039/D5EB00064E

structure transformations that enhance ionic conductivity. For example, by introducing partial In^{3+} into Li_3YCl_6, the crystal structure of $Li_3Y_{1-x}In_xCl_6$ ($0<x<1$) can change from hcp-cubic phase to hcp-trigonal phase (**Figure 4c**).[59] When x exceeds 0.2, it can transform into ccp-monoclinic phase with the ionic conductivity increased to 10^{-3} S cm^{-1}, indicating that the conversion of the sublattice plays a key role in promoting Li^+ transport. Isovalent cation substitution can also increase the vacancy concentration, allowing ions to hop more easily between these vacancies for rapid conduction. In the $Li_2In_xSc_{0.666-x}Cl_4$, the In doping significantly enhanced ionic conductivity, reaching up to 2.03×10^{-3} S cm^{-1}.[88] This is attributable to the increased disorder of Li^+ distribution and the additional vacancies generated that facilitate Li^+ migration. Although the overall crystal structures remain almost unchanged after doping, the alteration in Li occupancy forms a three-dimensional transport network that not only enhances the ionic conduction but also reduces the electronic conduction.

In addition to isovalent doping, aliovalent doping can also enhance ionic conductivity by altering carrier concentration/distribution, defect concentration, and local structures. Two common approaches including substituting low-valence metal cations with high-valence metal cations (Ta^{5+}, Nb^{5+}, Hf^{4+}, Zr^{4+}, etc.) to increase vacancy concentration, or substituting high-valence metal cations with low-valence ones (Fe^{3+}, In^{3+}, etc.) to increase carrier concentration and promote ion transport. A widely studied system involves using the cost-effective Zr^{4+} to replace trivalent metal cations, forming $Li_{3-x}M_{1-x}Zr_xCl_6$ (M=Y, Er; x=0-0.6).[85] The ionic conductivity can reach up to 1.4×10^{-3} S cm^{-1} compared to 10^{-5} S cm^{-1} for pristine Li_3YCl_6. The substitution induces a structural transformation from trigonal to orthorhombic, and the improvement in ionic conductivity is attributed to the vacancies introduced by Zr doping, which facilitates a three-dimensional transport network (**Figure 4d**). Additionally, the introduction of extra tetrahedral Li sites is able to construct a more favorable Li^+ transport framework. Similarly, there is the solid solution of $Li_3In_{1-x}Zr_xCl_6$ formed by the substitution of In^{3+} with Zr^{4+}.[89] This substitution not only generate additional lithium tetrahedral sites and vacancies, but also induce cation disorder and local structural distortions, promoting the formation of a three-dimensional Li^+ transport pathway. This significantly increases

the ionic conductivity to 1.25×10^{-3} S cm^{-1}. Another example is the replacement of Yb^{3+} with Hf^{4+} in Li_3YbCl_6, which results in a structural transformation from orthorhombic phase to monoclinic phase, favoring for the Li^+ diffusion.[90]

Furthermore, Mo and colleagues used high-throughput computational to analyze the ionic conduction in various aliovalent element-substituted chloride-based electrolytes (**Figure 4e**).[86] Their study reveals the influence of Li content and cation sublattice on Li^+ conduction. They proposed that reducing lithium octahedral occupancy to 40%-60%, lowering the cation concentration, and increasing cation spacing to achieve a sparse cation distribution could further enhance Li^+ conductivity. The high-valence cation substitution approach is also applicable to Na-based halide electrolytes. For example, substituting Y^{3+} or Er^{3+} with Zr^{4+} in $Na_{2.125}Y_{0.125}Zr_{0.875}Cl_6$ and $Na_{2.4}Er_{0.4}Zr_{0.6}Cl_6$ can significantly improve the ionic conductivity, although the values are still remained around 10^{-5} S cm^{-1}.[42, 43] The enhancement is mainly attributed to the increased vacancy concentration and the cooperative effect of multi-anion rotation with Na^+. Additionally, Fu et al. synthesized a UCl_3-type $Na_{1-x}La_{1-x}Zr_xCl_4$ electrolyte by replacing La^{3+} with Zr^{4+}, achieving an ionic conductivity of 2.9×10^{-4} S cm^{-1}.[77] This improvement primarily because Zr doping shortens the M–Cl bond length, expands the one-dimensional diffusion channel, and lowers the migration energy barrier, thereby enhancing the ionic conductivity. However, the presence of a small amount of La in the diffusion channel due to anti-site occupation with Na may hinder Na^+ diffusion. On the other hand, using low-valence cations such as Fe^{3+}, In^{3+}, and Sc^{3+} to replace the high-valence Zr^{4+} in $Li_{2+x}Zr_{1-x}M_xCl_6$ (M = In, Sc, Fe) resulted in electrolyte materials with high ionic conductivity (>10^{-3} S cm^{-1}).[91, 92] This enhancement is attributed to the increased Li^+ concentration and the expansion of the lattice volume caused by the dopants.

4.2 Anion modification

Similar to cation substitution, both isovalent and aliovalent anion substitution can alter the structure and even induce amorphous phases, thereby affecting the ionic conductivity. Different anions have distinct ionic radii and electron cloud distributions,

which lead to changes in lattice parameters upon substitution. Even with the same central cation, halide solid electrolytes can exhibit different crystalline structures with different anions. For example, Li_3YCl_6 is a trigonal phase, whereas Li_3YBr_6 is a monoclinic phase.[34] Moreover, larger anion radii and higher anion polarizability can expand the lattice spacing to create a 'softer' lattice environment that lowers the Li^+/Na^+ migration barrier although at the expense of reduced oxidative stability.

Mixing different halide anions can also have a significant impact on both the crystal structure and ionic conductivity. Yamada and colleagues were the first to study the effect of anion substitution on the conductivity of $Li_3InBr_{6-x}Cl_x$.[93] Replacing Br with Cl will reduce the lattice volume and lower the phase transition temperature. Although the reduced lattice volume typically diminishes ionic conductivity, this substitution in $Li_3InBr_{6-x}Cl_x$ enhances the ionic conductivity, primarily due to the ordered replacement of Cl, which altered the crystal symmetry or local environment to form a structure more favorable for ion transport. Similarly, Chen's group also improved the ionic conductivity of $Li_3Y(Br_3Cl_3)$ to 7.2×10^{-3} S cm^{-1} through Cl and Br anion mixing combined with hot pressing.[94] This improvement is attributed to the Li exsiting in both octahedral and tetrahedral sites, where the tetrahedral Li sites facilitate the formation of vacancies in the octahedral sites, thereby lowering the activation energy for Li^+ migration. Meanwhile, the hot pressing also optimizes the grain boundaries, so that both effects contribute together to enhance the Li^+ conduction. In addition, there are many other studies reported the high ionic conductivities in dual-halide anion-mixed electrolytes, such as $Li_3YCl_{4.5}Br_{1.5}$ (6.1×10^{-3} S cm^{-1}),[95] $Li_3GdCl_3Br_3$ (11×10^{-3} S cm^{-1}),[95] and $Li_3HoBr_3I_3$ (2.7×10^{-3} S cm^{-1}).[96]

For Na-based halide electrolytes, computational predictions suggest that mixing Br and I anions to induce local structural disorder could raise the ionic conductivity of $Na_3GdBr_3I_3$ to 7.5×10^{-3} S cm^{-1}, although this compound has not yet been experimentally synthesized.[97] Furthermore, introducing F^- into the lattice produces an effect opposite to that of Cl, Br, and I. They will slightly reduce the ionic conductivity but broaden the oxidation stability window. This behavior is related to the intrinsic properties of the anions, such as ionic radius and electronegativity. For example, the dual-halogen SE

with fluorinated compounds such as $Li_2ZrCl_xF_{6-x}$[98, 99] and $Li_3InCl_{4.8}F_{1.2}$[100] can exhibit superior oxidative stability up to even 6 V (vs. Li^+/Li), which is beneficial to the compatibility with high-voltage cathode and enhanced energy density.

Due to the differences in valence, ionic radius, and electronegativity between oxide and chloride ions, oxygen doping can induce lattice distortions that alter the size and connectivity of ion diffusion channels and in some cases even cause the structure to become amorphous. For example, Jung et al. synthesized a high-ionic-conductivity nanocomposite solid electrolyte (HNSE), ZrO_2(-ACl)-A_2ZrCl_6 (A= Li or Na), via a two-step ball milling process (**Figure 5a**).[101] Although the HNSE structure contains the ion-insulating ZrO_2 phase, the nanometer-scale ZrO_2 particles are dispersed within the Li_2ZrCl_6 matrix, creating numerous interfaces that serve as fast ion transport pathways. The conduction behavior at the ZrO_2/Li_2ZrCl_6 interfaces is attributed to the local substitution of oxygen ion, which widens the ion transport channels and increases the Li content at the interface.

This section will mainly describe crystalline oxyhalide electrolytes, while the amorphous oxyhalide electrolytes will be discussed in detail in **Section 4.3**. Tanaka's group fabricated orthorhombic $LiMOCl_4$ (M= Nb, Ta) via ball milling with subsequent sintering, achieving a superior room-temperature ionic conductivities exceeding 10×10^{-3} S cm^{-1} as well as a high oxidative stability window of 5 V vs. Li^+/Li.[38] Furthermore, a series of low-cost Zr-based oxychloride electrolytes have been reported, including $Li_3Zr_{0.75}OCl_4$,[102] $Li_{2.22}Zr_{1.11}O_{0.67}Cl_{5.33}$[103] and $Li_{3.1}ZrCl_{4.9}O_{1.1}$,[104] all of which exhibit the monoclinic structures and the ionic conductivities exceeding 10^{-3} S cm^{-1}. $Li_3Zr_{0.75}OCl_4$ is synthesized by substituting the Sc^{3+} with 0.75 Zr^{4+} in Li_3ScCl_6 and compensating for the cation vacancies by replacing a small amount of Cl with O (**Figure 5b**).[102] The non-periodic features and crystalline phase (monoclinic structure) synergistically promote the ion conduction and facilitate Li^+ transport. Similarly, $Li_{2.22}Zr_{1.11}O_{0.67}Cl_{5.33}$ and $Li_{3.1}ZrCl_{4.9}O_{1.1}$ are both produced via oxygen substitution that induces a phase transformation from trigonal to monoclinic structure, which stabilizes the tetrahedral lithium sites and shortens the Li^+ hopping distance to enhance the conductivity.

View Article Online
DOI: 10.1039/D5EB00064E

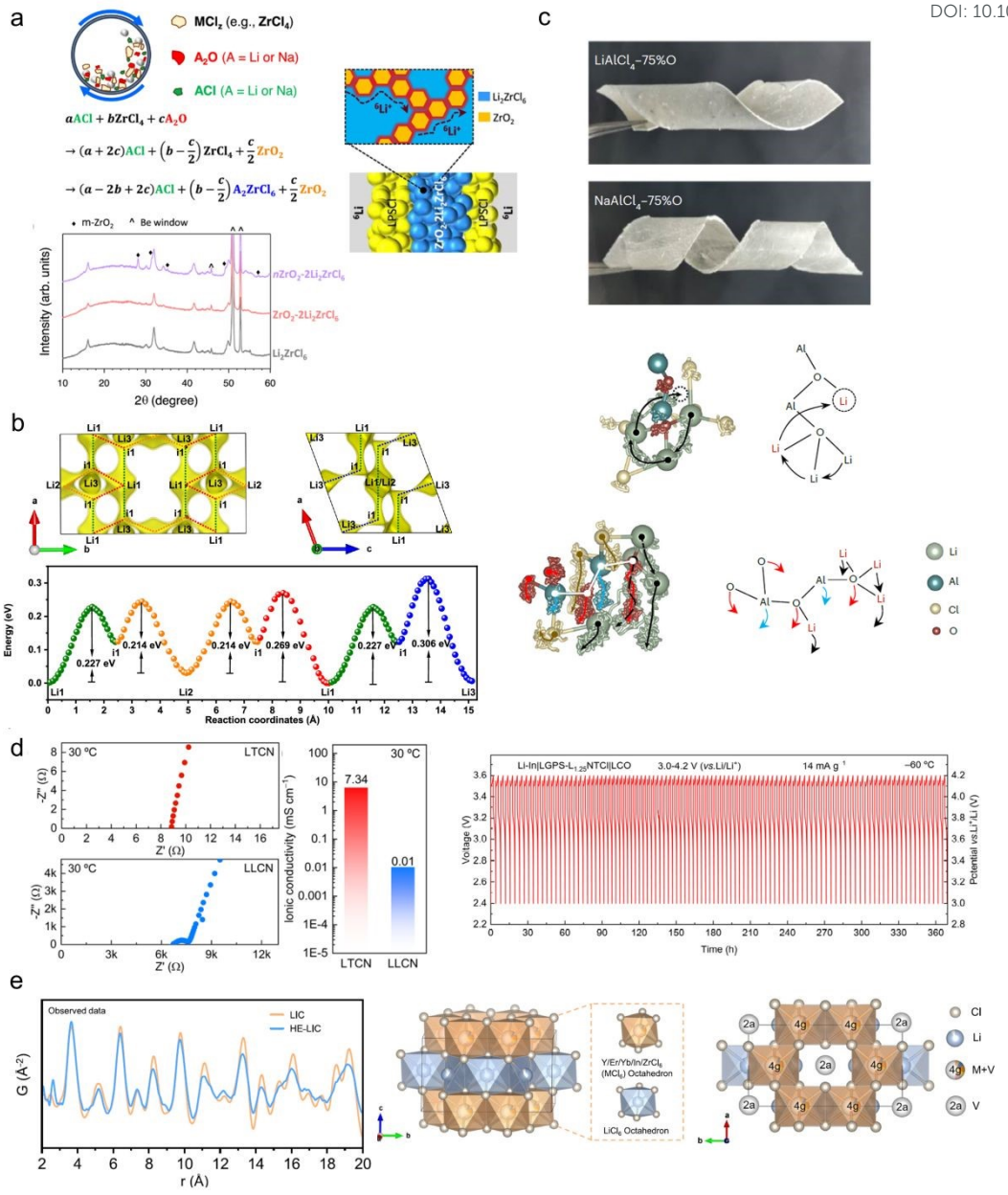

Figure 5. (a) ZrO_2(-ACl)-A_2ZrCl_6 (A= Li or Na) through two-step ball-milling synthesis method, and the schematic diagram of the interfacial superionic Li^+ diffusion pathways.[101] (b) Li^+ migration pathways and migration energy barriers in $Li_3Zr_{0.75}OCl_4$.[102] (c) The hopping and migrate of Li^+ in the viscoelastic electrolytes of LACO and NACO.[39] (d) The high ionic conductivity and excellent extremely low temperatures performance of amorphous nitrogen-halide electrolytes $Li_{3x}TaCl_5N_x$.[105, 106] (e) The local structure and unit cell of HE-LIC.[107]

4.3 Amorphization

Amorphization is another efficient strategy to improve the carrier transport by abundant intrinsic defects, few grain boundaries, and large transport spaces. There are various strategies can make the halide-based electrolyte with amorphous structures such

View Article Online
DOI: 10.1039/D5EB00064E

as extending the mechanochemical process as mentioned in the previous section, or introducing divalent oxygen or trivalent nitrogen into halides, thereby enhancing the ionic conductivity

Oxyhalides have emerged as a promising solid electrolyte system over the past three years, exhibiting unique structural and performance advantages. Oxygen element plays a critically role due to its strong ability to form amorphous structures, and preferentially connecting metal polyhedrons over short distances in the form of bridging oxygen, which contributes to high ionic conductivity. Currently, oxyhalide electrolytes are mainly reported based on the metal cations such as Al, Ta, Nb, Hf and Zr, as well as antiperovskite structures Li/Na_3OX (X=Cl, Br, I).

Our group first proposed a class of viscoelastic inorganic glass electrolytes (VIGLAS) with aluminum-based compounds $LiAlCl_{4-2x}O_x$ (LACO) and $NaAlCl_{4-2x}O_x$ (NACO), whose ionic conductivities are 1.52×10^{-3} S cm^{-1} and 1.33×10^{-3} S cm^{-1}, respectively.[39] By introducing varying amounts of oxygen element to sodium/lithium tetrachloroaluminate to replace part of Cl with O, the materials transformed from a brittle molten salt into a ductile glass at room temperature as the oxygen content increased, as shown in **Figure 5c**. The high ionic conductivity is attributed to the introduced O shortens the distance between Li–Li, allowing Li^+ to hop in a shorter distance. On the other hand, the vibration of the Al–O–Al chains will facilitate the simultaneous migration of surrounding Li^+ and Cl^-, thus promoting ion transport. Moreover, all the elements involved in the VIGLAS are earth-abundant elements, so that the materials have the lowest cost compared to other reported inorganic SEs. This finding is a milestone that simultaneously achieved the merits of inorganic and polymer electrolytes, which has gained wide recognition from researchers.[108-110] Subsequently, Sun's group synthesized a series of amorphous $LiAlO_xCl_y$ electrolytes with the ionic conductivity exceeding 10^{-3} S cm^{-1} using different methods, such as self-propagating method (simply pressing followed by sintering), crystal water-assisted method (using $LiCl–AlCl_3–AlCl_3\cdot6H_2O$), and low-temperature sintering of Li_2O_2 with $AlCl_3$.[111-113] Nazar and colleagues also prepared a aluminum-based oxychloride electrolyte ($LiAlCl_4–AlCl_3–AlCl_3\cdot6H_2O$) with plasticity via solid-state sintering.[114] This method

View Article Online
DOI: 10.1039/D5EB00064E

can also be extended to Na^+ conductors and Na–K mixed ion conductors.

Furthermore, there are various other reported amorphous oxyhalide electrolytes $Li/NaMO_xCl_y$ (M = Ta, Nb, Hf, Zr) with high ionic conductivity ranging from 10^{-4} to 10^{-3} S cm^{-1} by supplying an oxygen source through different oxygen-containing lithium or sodium salts (e.g., Li_2O, Li_2O_2/Na_2O_2, LiOH/NaOH) via ball milling or sintering, as shown in **Table 2**. In addition, $Li_{2.5}ZrCl_5F_{0.5}O_{0.5}$ synthesized by dual doping with fluoride and oxide anions into Li_2ZrCl_6 exhibits a high ionic conductivity of 1.17×10^{-3} S cm^{-1} and excellent voltage stability (up to 4.87 V vs. Li^+/Li).[115] In this case, the incorporation of F improves high-voltage stability, while the introduction of O induces the structure toward amorphization and reduces crystallinity to 24.6%. This disordered structure mitigates the negative impact of F on conductivity.

Table 2. Amorphous oxyhalide electrolytes with different oxygen source.

Oxyhalide electrolytes	Oxygen source	Conductivity (mS cm^{-1})	Ref.
$LiAlCl_{2.5}O_{0.75}$	Sb_2O_3	1.52	39
$NaAlCl_{2.5}O_{0.75}$	Sb_2O_3	1.33	39
AlOCl-nanoLiCl	Li_2O_2	1.02	113
LiAlOCl-981	$AlCl_3\cdot6H_2O$	1.04	112
AOC-2LiCl	Sb_2O_3	1.24	111
$PLAOC^{0.3b}$	$AlCl_3\cdot6H_2O$	1.3	114
$1.6Li_2O\text{-}TaCl_5$	Li_2O	6.6	37
$1.6Li_2O\text{-}HfCl_4$	Li_2O	1.97	37
$NaTaOCl_4$	NaOH	1.2	44
$Na_2O_2\text{-}HfCl_4$	Na_2O_2	0.52	80
$Na_2O_2\text{-}ZrCl_4$	Na_2O_2	0.42	80
$Na_2O_2\text{-}TaCl_5$	Na_2O_2	2	80
$0.5Na_2O_2\text{-}TaCl_5$	Na_2O_2	4.62	116
$Li_{2.5}ZrCl_5F_{0.5}O_{0.5}$	Li_2O	1.17	115

Beyond the oxygen substitution, nitrogen doping can also induce the formation of

View Article Online
DOI: 10.1039/D5EB00064E

an amorphous phase. Han et al. reported a class of amorphous nitrogen-halide electrolytes $Li_{3x}TaCl_5N_x$ with high ionic conductivities up to 7.34×10^{-3} S cm^{-1} (**Figure 5d**).[106] This improvement is mainly due to the introduction of nitrogen altering the coordination environment between cations and anions, thereby facilitating the Li^+ transport. This electrolyte also exhibits excellent performance under extremely low temperatures, maintaining stable charge/discharge cycles for over 200 hours at –60 °C.[105]

4.4 Designing high-entropy configuration

High-entropy materials typically consist of five or more metal elements and have a configuration entropy $\Delta S \geq 1.5R$ (R is the ideal gas constant). High-entropy strategy can promote disorder in the arrangement of Li^+ and vacancies, locally disrupting site energy by introducing disorder and distortion, which make the energy levels of adjacent sites to overlap and therefore reduce the activation energy. Typically, metal cations with similar ionic radii but varied valence states are selected to facilitate the formation of solid solutions. Currently, research on high-entropy halide electrolytes is still in early stages, and only a few materials have been reported. For example, Luo and colleagues synthesized a high-entropy electrolyte $Li_{2.75}Y_{0.16}Er_{0.16}Yb_{0.16}In_{0.25}Zr_{0.25}Cl_6$, which exhibits an ionic conductivity of 1.71×10^{-3} S cm^{-1}.[107] The introduction of multiple cations with different radii leads to lattice distortions that increase the migration pathways for Li^+. In addition, the incorporation of high-valence Zr introduces more lithium vacancies, and the increased Li–Cl bond length makes them more prone to break, thereby forming active sites for Li^+ migration (**Figure 5e**). Moreover, the restricted vibrational range of Cl^- reduces spatial hindrance. These combined factors make this high-entropy material high ionic conductivity. Similarly, Yang's group employed a high-entropy strategy to simultaneously enhance the high-voltage stability (up to 4.8 V vs. Li^+/Li) and ionic conductivity of halide electrolytes.[117] They synthesized a $Li_{2.9}In_{0.75}Zr_{0.1}Sc_{0.05}Er_{0.05}Y_{0.05}Cl_6$ electrolyte with an ionic conductivity of up to 2.18×10^{-3} S cm^{-1}, and proposed that increasing configuration entropy and reducing oxidative by-products can effectively enhance the oxidation stability.

View Article Online
DOI: 10.1039/D5EB00064E

5. Chemical and electrochemical stability of halide-based electrolytes

5.1 Air/Humidity stability

In recent years, halide-based electrolytes have primarily focused on enhancing ionic conductivity and electrochemical stability, as well as exploring the optimization of ion transport mechanisms. However, due to the high hygroscopicity and deliquescence of halide-based electrolytes and their raw materials, their synthesis must be strictly rely on an inert atmosphere. In addition, the degradation products of halide-based electrolytes are highly corrosive, which significantly increases the industrial costs and technical complexity. Furthermore, the moisture-induced degradation process involves a complex, multiscale gas-solid interfacial reaction network, and a systematic understanding of the interaction mechanisms between halide-based electrolytes and air is still lacking.

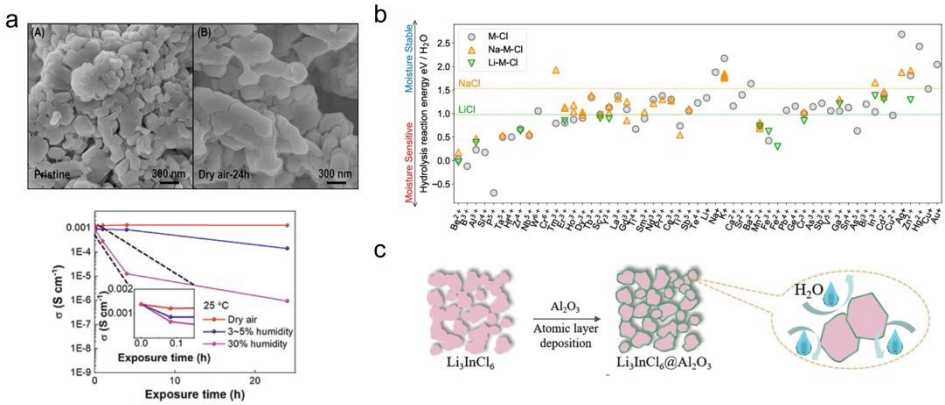

Figure 6. (a) The particle morphology and ionic conductivity of Li_3InCl_6 in dry and humid environments.[118] (b) Computational analyses of hydrolysis reaction energies in Li/Na-based ternary chlorides.[119] (c) Schematic diagram showing the deposition of an Al_2O_3 coating on Li_3InCl_6 via atomic layer deposition.[120]

Li_3InCl_6 is recognized as one of the most air-stable electrolytes and can even be directly synthesized via aqueous solution method. However, as shown in **Figure 6a**, in dry air, Li_3InCl_6 shows no significant changes in particle morphology and ionic conductivity within 24 h.[118] As ambient humidity increases, its ionic conductivity declines markedly. Particularly, when the humidity reaches 30%, the ionic conductivity rapidly drops to 10^{-6} S cm^{-1} and the activation energy increases, indicating that Li^+ transport becomes more difficult. This is because that Li_3InCl_6 reacts with the moisture

in the air to form In_2O_3, LiCl, and HCl. It can also absorb water to form the hydrate $Li_3InCl_6 \cdot xH_2O$, which reduces its ionic conductivity. Consequently, Li_3InCl_6 exhibits better air stability in low-humidity environments or dry room, and the hydrate $Li_3InCl_6 \cdot xH_2O$ formed upon water absorption is reversible with Li_3InCl_6. Once the crystallization water is removed via vacuum drying, the ionic conductivity can be fully restored.[35] So far, this is the only halide-based electrolyte can directly form a hydrate intermediate and undergo reversible chemical transformation. Other halide-based electrolytes decompose directly into $MCl_y \cdot xH_2O$ and $LiCl \cdot xH_2O$, where $MCl_y \cdot xH_2O$ further decomposes into M_2O_3 and HCl during dehydration.[120, 121] Similarly, in $Li_3Y_{1-x}In_xCl_6$ where In^{3+} partially substitutes for Y^{3+}, increasing the substitution level transforms the electrolyte's structure from hcp to ccp anion sublattice, thereby improving the moisture resistance.[59] This is primarily because the ccp-type $Li_3Y_{1-x}In_xCl_6$ will first forms a hydrate intermediate $Li_3Y_{1-x}In_xCl_6 \cdot H_2O$ after absorbing water, which can be reversibly converted back to $Li_3Y_{1-x}In_xCl_6$ upon high-temperature dehydration. Additionally, computational analysis of hydrolysis reaction energies have shown that in lithium-based ternary chlorides, cations such as In^{3+}, Ga^{3+}, Zn^{2+}, and Cd^{2+} exhibit excellent moisture resistance, while in sodium-based ternary chlorides, lanthanide cations like Tm^{3+} and Tb^{3+} provide good moisture resistance (**Figure 6b**).[119] Ma et al. found that Li_2ZrCl_6 also has good moisture resistance even after being exposed to a nitrogen environment with 5% humidity for 24 h.[36] Its structure remained unchanged and the ionic conductivity could still kept at 0.81×10^{-3} S cm^{-1}. However, in contrast to Li_2ZrCl_6, Li_3InCl_6 quickly formed hydrates under the same conditions, resulting in a one-order-of-magnitude drop in ionic conductivity. Beyond synthesizing halide-based electrolytes that are intrinsically resistant to air and moisture, the issue can also be mitigated by adjusting the contact area and composition of the solid–gas interface. For example, depositing a layer of Al_2O_3 on Li_3InCl_6 effectively isolates the electrolyte from direct contact with air, greatly enhancing its air stability (**Figure 6c**).[120] Currently, strategies to improve the air/moisture stability of halide-based electrolytes are relatively limited, and more explorations are expected in the future.

View Article Online
DOI: 10.1039/D5EB00064E

5.2 Intrinsic electrochemical stability

The electrochemical stability window (ESW) of halide-based electrolytes is a key parameter affecting the electrochemical performance of ASSBs. Depending on the halide anions, the order of ESW width is generally determined as F > Cl > Br > I. Both theoretical calculations and experimental data have demonstrated that fluoride- and chloride-based electrolytes exhibit high oxidation stability, exceeding 6 V vs. Li^+/Li and 4 V vs. Li^+/Li, respectively (**Figure 7a**).[75] For the Na–M–X (X = F, Cl, Br, I, O, S), thermodynamic calculations of the intrinsic ESW for the various anions in the structure indicate that nearly all such electrolytes exhibit oxidation stability over 3 V vs. Na^+/Na, except for iodide-based electrolytes (**Figure 7b**).[122] For example, the electrochemical windows of Na_3YCl_6 and Na_3YBr_6 are 0.51-3.75 V vs. Na^+/Na and 0.57-3.36 V vs. Na^+/Na, respectively.[122] However, halide-based electrolytes also suffer from a critical drawback that the electrochemical reduction stability is relatively poor. Their high reduction potentials make them unsuitable for direct contact with metallic lithium or sodium anodes. The extent to which the reduction potential is limited mainly depends on the reduction potential of the central metal cations. Thermodynamic calculations have shown that group IIIB cations (such as Sc^{3+} and Y^{3+}) exhibit relatively good reduction stability.[123] It is worth noting that in practical applications, the formation of effective interfacial passivation layers and favorable interfacial kinetics can also result in an actual ESW that surpasses the theoretical stability limits, which should be considered integrally.

5.3 Interfacial stability

In addition to the important influence of the intrinsic properties of halide-based electrolytes, the poor interfacial contact with electrode materials and the issues with interfacial chemical stability are also the key factors limiting their development. Unlike the good wettability of liquid electrolytes, the contact between SEs and electrode materials is point contact, resulting in a small contact area that leads to high interfacial resistance and directly reduces the migration pathways for Li^+/Na^+ while causing stress accumulation. Moreover, when the electrode potential exceeds the electrolyte's

intrinsic electrochemical stability window, spontaneous interfacial reactions will occur. There are three different types of interfaces that can be formed between electrodes and electrolytes (**Figure 7c**). The first is that the electrolyte and electrode are thermodynamically stable, indicating that no reaction occurs to form interfacial components. The second is that although the electrode and electrolyte are not thermodynamically stable, the generated interfacial components are ionic conductive and electronic insulating. The third type is the interfacial components within mixed electronic and ionic conductor, which leads to continuous reactions until the electrolyte is completely consumed, and obviously, should be strictly avoided. In practice, the first type of the interface is hardly to be achieved especially at the anode side since metallic lithium or sodium anodes have the lowest chemical potentials. The second-type interface is the most possible one, where a passivation layer can form to extend the ESW of the electrolyte.

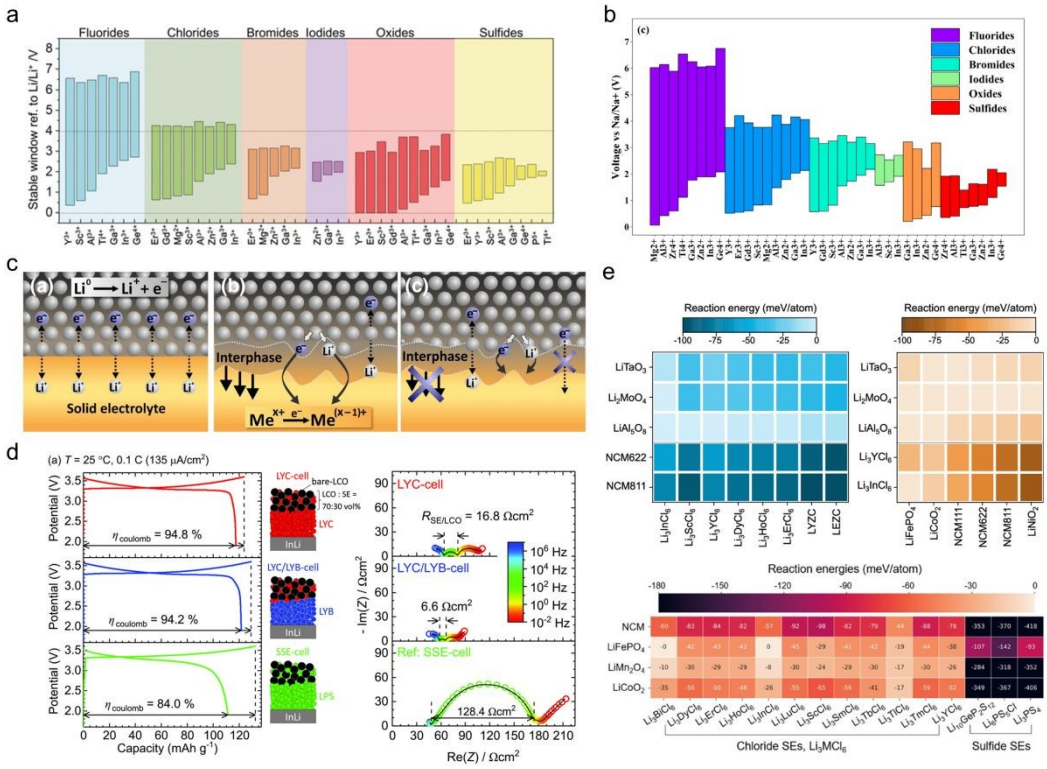

Figure 7. The thermodynamic electrochemical windows of (a) Li-M-X (X= F, Cl, Br, I, O, S)[75] and (b) Na-M-X through calculation.[122] (c) Three types of interfaces between lithium metal and solid electrolytes.[124] (d) Initial charge/discharge curves and the impedance value of Li_3YCl_6 after the first charging cycling.[34] (e) The reaction energy calculations between different cathode materials and halide electrolytes based on various metal cations.[123, 125]

Due to the high oxidative stability of halide-based electrolytes, it can typically be directly in contact with oxide cathodes without additional surface coatings. Asano et al. first matched Li_3YCl_6 with uncoated $LiCoO_2$ achieving an initial Coulombic efficiency as high as 94.8% and a low interfacial resistance of 16 Ω/cm^2 (**Figure 7d**).[34] In addition, cathodes such as $LiNi_{0.6}Mn_{0.2}Co_{0.2}O_2$, $LiNi_{0.8}Mn_{0.1}Co_{0.1}O_2$, $LiNi_{0.83}Mn_{0.05}Co_{0.12}O_2$ and $LiNi_{0.88}Al_{0.01}Co_{0.11}O_2$ have also been reported to be compatible with halide-based electrolytes.[69, 92, 126-128] However, cathode active materials with different structures and varying transition metal contents exhibit significant differences in interfacial stability with halide-based electrolytes (**Figure 7e**).[123, 125] For example, tantalum-based oxychloride electrolyte (LTOC) paired with Ni-rich NCM83 cathodes shows optimal compatibility although the LTOC/NCM83 interface is thermodynamically unstable (**Figure 8a**).[129] This is due to the formation of a functional interfacial passivation layer (e.g. Li-Ta-O compounds) suppresses further decomposition. In contrast, when LTOC is matched with $LiCoO_2$ cathode, inter-diffusion of Co and Ta occurs at the interface, and the generated byproducts such as Ta_2CoO_6 leads to instability of the interface. Lowering the operating temperature can reduce the reactivity of these interfacial reactions. Moreover, the physical contact between the halide-based electrolyte and the cathode particles significantly affects the electrochemical performance. A well-designed composite cathode with an appropriate composition ratio and uniform mixing of the active cathode material and catholyte is one of the key factors in constructing a continuous interlinked network for both ion and electron diffusion. The contact morphology and microstructure among the composite cathode particles can greatly influence the electrochemical performance of ASSBs. During electrochemical cycling, the cathode active material typically undergoes volume changes due to variations in Li/Na content, which generates internal stress and results in a loss of contact between the electrolyte and the cathode active particles, thereby degrading cycling stability. Compared with polycrystalline cathode active materials, monocrystal cathodes offer better high-voltage tolerance and higher mechanical stability, which can help prevent contact loss in composite cathodes. In contrast, polycrystalline cathode particles are prone to particle breakage during the preparation and compaction processes, and they

View Article Online
DOI: 10.1039/D5EB00064E

also exhibit anisotropic volume strain during cycling, leading to intergranular cracks that will reduce the ion transport kinetics and increase the interfacial impedance. For example, Jung's group investigated the performance differences between monocrystal and polycrystalline Ni-rich oxide cathodes (NCA) paired with Li_3YCl_6 in ASSBs (**Figure 8b**).[127] They found that the combination of monocrystal NCA with Li_3YCl_6 achieved stable long-term cycling with a capacity retention of 96.8% after 200 cycles. This outstanding performance is mainly attributed to the dense, grain-boundary-free structure of the monocrystal materials, which significantly enhances its resistance to volume strain, while the morphology of the monocrystal particles prevents local stress concentration caused by particle agglomeration. **Table 3** and **Table 4** respectively summarize the typical cathode compositions and electrochemical performances of current Li- and Na-based halide electrolytes, offering an intuitive view of their development at this stage.

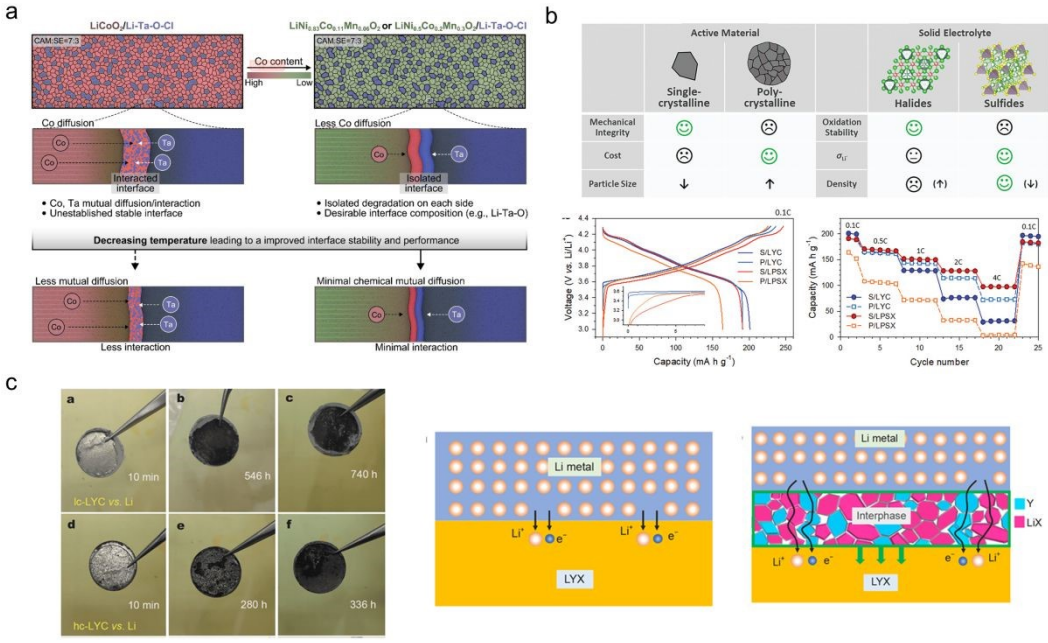

Figure 8. (a) Schematic diagram of the interface between LTOC and cathode materials with different Co contents at different temperatures.[129] (b) Effect of monocrystal and polycrystalline cathodes on compatibility with halide-based electrolytes.[127] (c) Interfacial reaction phenomena between Li_3YX_6 and metallic lithium anode.[130]

As mentioned above, most halide-based electrolytes exhibit poor reduction stability and are thermodynamically unstable with metallic lithium/sodium and alloy anodes (e.g., Li_xIn, Na_xSn). Therefore, understanding the reaction mechanisms between

these electrolytes and the anodes is of utmost importance. For example, Ma et al. investigated the reaction mechanism between Li_3YX_6 (X = Cl, Br) and metallic lithium anodes, founding that the thermodynamic incompatibility arises because Li_3YX_6 is reduced to form metal Y and LiX, creating an interfacial phase that is a mixed ionic and electronic conductor, which leads to a continuous interfacial reaction during the cycling (**Figure 8c**).[130] Similarly, Li_3InCl_6 reacts with metallic lithium to form LiCl and In. In the $Li|Li_3InCl_6|Li$ symmetric cell, the interfacial resistance was observed to continuously increase over time, and reaching a total resistance as high as 854 Ω after just one hour.[131]

The stability of halide-based electrolytes against anodes can be improved by constructing an interfacial buffer layer. Currently, the most commonly used method is to combine halide-based electrolytes with sulfides-based electrolytes (Li_6PS_5Cl, $Li_{10}GeP_2S_{12}$, Na_3PS_4, etc.) to form a dual-electrolyte layer, although it should be noted that interfacial instability also exists between halide-based and sulfide-based electrolytes.[106, 112, 116] Besides sulfide-based electrolytes, nitride-based electrolytes have also been demonstrated to be effective as modification layers. The vacancy-rich β-Li_3N[132] and $Li_9N_2Cl_3$[133] and the oxyhalide nitride solid electrolyte $Li_xN_yI_z$-qLiOH[134] reported both show high stability to metallic lithium anodes, which achieved long-term stable lithium plating/stripping. Moreover, owing to their softer sublattice and lower reduction potential, iodide-based electrolytes such as cubic Li_4YI_7 also show good compatibility with lithium metal.[135] At present, only a few halide-based electrolytes have achieved stability on the anode side, but cannot achieve stability on both cathode and anode materials at the same time. They still need to be used in combination with other oxidation-resistant halide-based electrolytes.

6. Advanced Characterization Techniques

Developing high-performance halide-based electrolytes requires an in-depth understanding of their structures, ion diffusion pathways, and transport mechanisms. Moreover, to realize commercially viable halide-based solid-state batteries, it is also crucial to investigate the evolution and degradation of the internal structures and

View Article Online
DOI: 10.1039/D5EB00064E

interfaces of halide-based electrolytes during cycling. Electrochemical characterization forms the foundation for understanding solid-state battery materials. In addition, a variety of advanced in situ and ex situ characterization techniques can be employed to study the structural, morphological, and other properties of solid-state electrolytes and their interfaces with electrodes. Beyond experimental techniques, computational methods such as density functional theory (DFT), ab initio molecular dynamics (AIMD) and bond valence sum evaluation (BVSE) can be used to simulate structures and Li^+/Na^+ transport pathways within electrolytes, providing further support for experimental findings. The following section outlines several advanced characterization techniques used to describe structural information in halide-based electrolytes.

X-ray diffraction (XRD) performs exceptionally well in detecting heavy atoms such as metals or halogens, but it is relatively insensitive to light elements. In contrast, neutron powder diffraction (NPD) plays an indispensable role in identifying the distribution and occupancy of light elements like Li^+/Na^+ in newly crystal structures, as well as in elucidating their migration pathways, due to its high sensitivity to light atoms.[136] For example, Yao et al.[71] used synchrotron X-ray diffraction to identify Ta, La, Cl, and particularly La/Ta vacancies to confirm the overall lattice framework in $Li_{0.388}Ta_{0.238}La_{0.475}Cl_3$. Meanwhile, neutron data were employed to determine the lithium distribution, revealing two distinct Li sites in the structure. Furthermore, based on the NPD determined structure, bond valence site energy (BVSE) analysis showed that lithium migrates not only along 1D channels but also between adjacent channels via La vacancies.

Pair distribution function (PDF) analysis is a powerful technique for resolving atomic-scale structures of halide-based electrolytes, particularly those that are amorphous or locally disordered. It reveals both short-range and medium-range order in materials, overcoming the limitation of the conventional XRD which only probes long-range order. PDF provides valuable information on average atomic pair distances within locally ordered units in amorphous phases. For instance, Sun et al.[41] used PDF analysis to show that with increasing ball-milling time of $NaTaCl_6$ -alongside increasing

ionic conductivity- the medium-range peak features (5-20 Å) gradually weakened, indicating the structure is more disordered. Meanwhile, an enhancement of Cl-Cl scattering (peaks at 3.5-4 Å) suggested a denser packing of $TaCl_6$ octahedra and the gradual formation of poly-($TaCl^+_6$) octahedral network, which constitutes a sodium conducting amorphous framework.

In addition, solid-state nuclear magnetic resonance (NMR) and X-ray absorption spectroscopy (XAS) are essential for probing local coordination and bonding environments. XAS can analyze bond length variations via Fourier-transformed R-space data, while solid-state NMR distinguishes local coordination environments through chemical shifts. Furthermore, 2D NMR spectroscopy can trace Li^+ migration pathways at the atomic level. For example, using 2D ^{7}Li EXSY exchange NMR, Sun's group discovered that the introduction of lithium carbonate promotes lithium exchange both between amorphous domains and between amorphous and crystalline phases in the oxyhalide-based AlOCl–2LiCl (LAOC) electrolyte.[137] This resulted in an accelerated movement of ions at various lithium sites, indicating an enhanced ion transport and an improved interface dynamics.

7. Conclusions and Outlooks

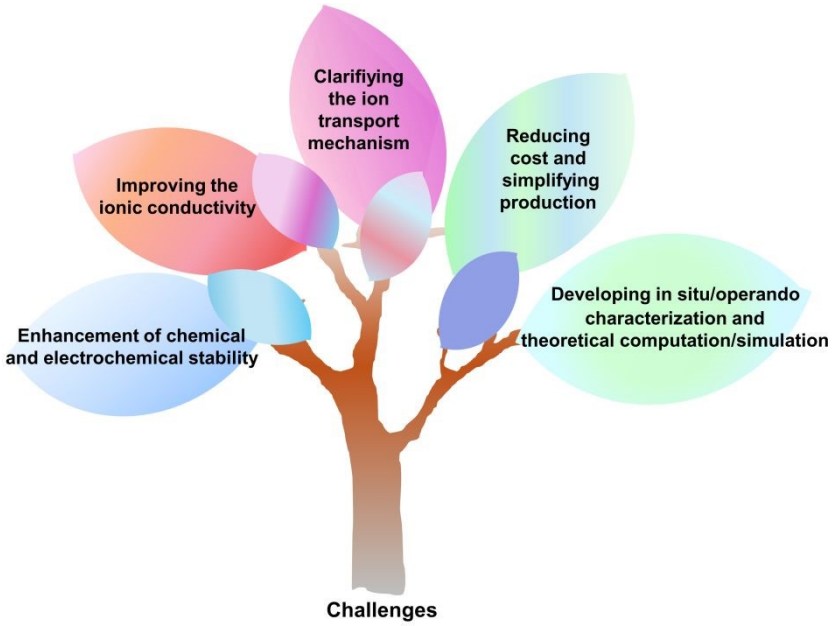

Figure 9. The schematic diagram of the challenges faced by halide-based electrolytes.

This review summarizes the latest progress in Li-based and Na-based halide

electrolytes. Firstly, it outlines the commonly used synthesis methods, which mainly include solid-state synthesis (mechanical milling, sintering and their combination) and liquid-phase synthesis (water-mediated and ammonium-assisted wet chemistry), with solid-state synthesis being predominant. Mechanical milling can induce local structural distortions and disorder to enhance ionic conductivity, while also ensuring a more uniform mixing of precursors, thereby reducing the sintering time. In contrast, among liquid-phase synthesis methods, only Li_3InCl_6 can be synthesized using a water-mediated approach, which cannot be generalized to other systems. Secondly, we classify the existing halide-based electrolytes into three categories based on structural differences, and we describe in detail the ion transport mechanisms through representative electrolyte materials. The structures are mainly composed of close-packed anion framework (ccp, hcp), non-close-packed anion framework of the UCl_3-type, and amorphous structures. The transport mechanism is primarily based on vacancy-mediated process. In addition, we provide a detailed overview of strategies for enhancing ionic conductivity and optimizing ion transport. Ionic conductivity can be effectively improved by doping with isovalent or aliovalent cations/anions, introducing vacancy defects or increasing carrier concentration, or conversing the structures into amorphous phases. Finally, we discuss the challenges and failure mechanisms faced by the air stability of halide-based electrolytes and the interfacial stability with both cathode and anode materials. The thermodynamic stability of halide-based electrolytes mainly depends on the oxidation potential, which is influenced by the anions, and the reduction potential that is affected by the central metal cations. In practical applications, interfacial stability is not only determined by the intrinsic electrochemical window but also by the stability of the interfacial products. While most halide-based electrolytes exhibit high oxidative stability, only a few are compatible with metallic lithium/sodium.

Despite the impressive progress in ionic conductivity and oxidative stability, halide-based electrolytes still face many practical challenges (**Figure 9**). First, the raw materials used for synthesizing halide-based electrolytes often involve expensive rare-earth elements, resulting in raised cost. Although more abundant and cheaper halide electrolytes based on elements such as Zr and Al have emerged merits in recent years,

which can achieve high ionic conductivity and low cost, these electrolytes are extremely sensitive to ambient humidity. They are prone to irreversible hydrolysis, which leads to structural degradation, a rapid decline in ionic conductivity, and corrosion of current collectors and casings, posing significant challenges for large-scale production. Moreover, the synthesis of halide-based electrolytes currently mainly relies on mechanical milling and solid-state sintering, with only Li_3InCl_6 being amenable to water-mediated liquid-phase synthesis. The complexity of the synthesis process further limits their scalability. Regarding the intrinsic properties of halide-based electrolytes, most Li-based halide electrolytes exhibit ionic conductivity around 10^{-3} S cm^{-1}, and there are also several materials can deliver very high ionic conductivity over 10^{-2} S cm^{-1}, which is comparable to liquid electrolytes. However, Na-based halide electrolytes generally have lower ionic conductivity and fewer available compositions. Due to the limitations in advanced characterization techniques, the ion transport mechanisms remain unclear, and the systematic understanding of the quantitative relationship between lattice dynamics and defect effects is lacking. These all still largely relies on computational simulations.

Furthermore, the solid-solid interface between halide-based electrolytes and the electrodes is still the most important problem, and the operation of the batteries requires a high external pressure. These require the deep understanding and rational design of viscoelastic electrolyte with high ionic conductivity to form the conformal interfaces and improve the solid-solid contact and interfacial ion transport. Besides, increasing the poor reduction stability of halide-based electrolyte is also an urgent task. This involves the consideration from both thermodynamic and dynamic aspects. In particular for all-solid-state Na batteries (ASSNBs), metallic sodium has not only poor cycling stability, but also has low melting point below 100 ℃ and is unstable even in dry air, which significantly limit the cycle life and enhance its safety hazard of ASSNBs in large-scale energy storage.[138] Therefore, more stable and safer anode such as hard carbons should be considered for the energy storage applications in ASSBs, whose interface with the halide-based electrolytes need to be further studied. Overall, current research indicates that halide-based electrolytes are still at their early stage, and many critical challenges

View Article Online
DOI: 10.1039/D5EB00064E

must be overcome before they can be put into practical industrial applications.

Table 3. Li-based halide electrolytes all-solid-state battery cell assembly parameters and electrochemical performances.

Halide-based electrolytes	Cathodes	Carbon addictive	Weight ratio of composite cathodes	Cathodes loading	Cycling pressure /MPa	Cycling temperature /°C	Cycling performance	Ref.
$LiAlCl_{2.5}O_{0.75}$	NCM622	CNT	20:70:5:5(PTFE)	4 mg cm^{-2}	-	60	Charged to 4.3 V at 1C and cycled for 600 times	39
$Li_{2.1}Zr_{0.95}Cu_{0.05}Cl_{4.4}O_{0.8}$	SC-NCM83	-	30:70	7-9 mg	75	25	Retained 90.3% capacity after 1000 cycles within a voltage range of 2.8-4.3 V at 2 C	139
$Li_{0.388}Ta_{0.238}La_{0.475}Cl_3$	SC-NCM523	VGCF	30:65:2:3(PTFE)	7.06 mg cm^{-2}	-	30	Li/$Li_{0.388}Ta_{0.238}La_{0.475}Cl_3$/NCM523 can be cycled for more than 100 cycles with 81.6% capacity retention	71
LiAlOCl-981	SC-NMC88	Carbon black	30:70:1	10 mg	200	25	Charged to 4.3 V at 0.5 C and sustained 84.86% capacity after 1500 cycles	112
$Li_{1.25}TaCl_5N_{0.417}$	LCO	VGCF	25:70:5	5 mg	0.5 ton	-20	Achieved a capacity retention of 83.13% after 1200 cycles at 1 C of –20 °C	106
$Li_{1.75}Zr_{0.75}Ta_{0.25}Cl_6$	NMC88	-	3:7	8.92 mg cm^{-2}	1.5 ton	25	Retained 90.6% of the initial capacity after 1600 cycles at 2C	140
$Li_{2.75}Y_{0.16}Er_{0.16}Yb_{0.16}In_{0.25}Zr_{0.25}Cl_6$	LCO	-	3:7	8 mg	-	25	Charged to 4.6 V and delivered an initial capacity as 185 mAh g^{-1} and maintained a capacity retention of 91.6% over 50 cycles	107

Table 4. Na-based halide electrolytes all-solid-state battery cell assembly parameters and electrochemical performances.

Halide-based electrolytes	Cathodes	Carbon addictive	Weight ratio of composite cathodes	Cathodes loading	Cycling pressure /MPa	Cycling temperature /°C	Cycling performance	Ref.
$NaAlCl_{2.5}O_{0.75}$	NVOPF	CNT	20:70:10:5(PTFE)	3.3 mg cm^{-2}	-	60	Charged to 4.3 V at 1C and cycled for 600 times with retention of 83.5%.	39
$0.5Na_2O_2$-$TaCl_5$	NMNFO	CNT	40:60,2wt%CNT	8 mg	80	25	Charged to 3.8 V and retained 66% capacity after 500 cycles at 0.1 C	116
Na_2O_2-$HfCl_4$	NMNFO	CNT	40:60,2wt%CNT)	8 mg	110	-	Maintained 78% capacity retention over 700 cycles at 0.2 C	80
2NaF-$ZrCl_4$	NFM	Super P	30:70, 5mg Super P	5.7 mg cm^{-2}	-	25	Charged to 4.3 V at 0.2 C and sustained 81.1% capacity after 600 cycles	141
$Na_{0.25}Y_{0.25}Zr_{0.75}Cl_4$	$NaCrO_2$	VGCF	16:11:0.5	-	50-70	23	Achieved a capacity retention of 83% after 500 cycles at 1 C	49
$Na_{0.7}Zr_{0.3}La_{0.7}Cl_4$	$NaCrO_2$	Super P	50:50:3	12 mg	-	30	Retained 88% of the initial capacity after 70 cycles at 0.3 C	77
$0.62[Na_{0.75}Sm_{1.75}Cl_6]$-$0.38[NaTaCl_6]$	NMNFO	Carbon black	40:60:2	7 mg	80	25	Showed capacity retention of 88.3% after 100 cycles at 0.2 C	78

View Article Online
DOI: 10.1039/D5EB00064E

Acknowledgements

This work was supported by the National Natural Science Foundation (NSFC) of China (52394170-52394174) and Young Elite Scientists Sponsorship Program by CAST (2024QNRC001).

References

1. C. Sun, J. Liu, Y. Gong, D. P. Wilkinson and J. Zhang, *Nano Energy*, 2017, **33**, 363-386.
2. J. B. Goodenough and K.-S. Park, *Journal of the American Chemical Society*, 2013, **135**, 1167-1176.
3. M. Liu, Z. Zeng, Y. Wu, W. Zhong, S. Lei, S. Cheng, J. Wen and J. Xie, *Energy Storage Materials*, 2024, **65**, 103133.
4. Y. Wang, X. Feng, W. Huang, X. He, L. Wang and M. Ouyang, *Advanced Energy Materials*, 2023, **13**, 2203841.
5. X. Feng, M. Ouyang, X. Liu, L. Lu, Y. Xia and X. He, *Energy Storage Materials*, 2018, **10**, 246-267.
6. X. Liu, D. Ren, H. Hsu, X. Feng, G.-L. Xu, M. Zhuang, H. Gao, L. Lu, X. Han, Z. Chu, J. Li, X. He, K. Amine and M. Ouyang, *Joule*, 2018, **2**, 2047-2064.
7. X. Tang, F. Xie, Y. Lu, Z. Chen, X. Li, H. Li, X. Huang, L. Chen, Y. Pan and Y.-S. Hu, *Nano Research*, 2023, **16**, 12579-12586.
8. J. Huang, K. Wu, G. Xu, M. Wu, S. Dou and C. Wu, *Chemical Society Reviews*, 2023, **52**, 4933-4995.

View Article Online
DOI: 10.1039/D5EB00064E

9. X. Tang, F. Xie, Y. Lu, H. Mao, Z. Chen, H. Pan, S. Weng, Y. Yang, X. Li, Z. Guo, Q. Guo, F. Ding, X. Hou, Y. Li, X. Wang, M.-M. Titirici, L. Chen, Y. Pan and Y.-S. Hu, *ACS Energy Letters*, 2024, **9**, 1158-1167.

10. H. Pan, Y.-S. Hu and L. Chen, *Energy & Environmental Science*, 2013, **6**, 2338-2360.

11. F. Li, Z. Wei, A. Manthiram, Y. Feng, J. Ma and L. Mai, *Journal of Materials Chemistry A*, 2019, **7**, 9406-9431.

12. A. Manthiram, X. Yu and S. Wang, *Nature Reviews Materials*, 2017, **2**, 16103.

13. Y.-K. Sun, *ACS Energy Letters*, 2020, **5**, 3221-3223.

14. H. Huo and J. Janek, *National Science Review*, 2023, **10**.

15. Y.-S. Hu and F. Xie, *ACS Energy Letters*, 2024, **9**, 6081-6083.

16. J. A. S. Oh, L. He, B. Chua, K. Zeng and L. Lu, *Energy Storage Materials*, 2021, **34**, 28-44.

17. C. Zhou, S. Bag and V. Thangadurai, *ACS Energy Letters*, 2018, **3**, 2181-2198.

18. Y. Yung-Fang Yu and J. T. Kummer, *Journal of Inorganic and Nuclear Chemistry*, 1967, **29**, 2453-2475.

19. D. Lee, A. Kumar Kakarla, S. Sun, P. Joohyun Kim and J. Choi, *ChemElectroChem*, 2025, **12**, e202400612.

20. A. C. Radjendirane, D. K. Maurya, J. Ren, H. Hou, H. Algadi, B. B. Xu, Z. Guo and S. Angaiah, *Langmuir*, 2024, **40**, 16690-16712.

21. Y. Yang, S. Yang, X. Xue, X. Zhang, Q. Li, Y. Yao, X. Rui, H. Pan and Y. Yu, *Advanced Materials*, 2024, **36**, 2308332.

22. Z. Jian, Y.-S. Hu, X. Ji and W. Chen, *Advanced Materials*, 2017, **29**, 1601925.

View Article Online
DOI: 10.1039/D5EB00064E

23. Y. Lu, J. A. Alonso, Q. Yi, L. Lu, Z. L. Wang and C. Sun, *Advanced Energy Materials*, 2019, **9**, 1901205.

24. H. Jia, L. Peng, C. Yu, L. Dong, S. Cheng and J. Xie, *Journal of Materials Chemistry A*, 2021, **9**, 5134-5148.

25. A. Hayashi, A. Sakuda and M. Tatsumisago, *Frontiers in Energy Research*, 2016, **4**.

26. M. Jin, D. Xu, Z. Su, Z. He, X. Chen, R. Wu and Y. Guo, *ACS Energy Letters*, 2024, **9**, 1176-1183.

27. J. Cuan, Y. Zhou, T. Zhou, S. Ling, K. Rui, Z. Guo, H. Liu and X. Yu, *Advanced Materials*, 2019, **31**, 1803533.

28. Z. Lu, J.-X. Kang, P. Qiu and X. Chen, *Batteries & Supercaps*, 2024, e202400636.

29. F. Gebert, J. Knott, R. Gorkin, S.-L. Chou and S.-X. Dou, *Energy Storage Materials*, 2021, **36**, 10-30.

30. Y. He, S. Yang, C. Liu, Y. Ouyang, Y. Li, H. Zhu, Y. Yao, H. Yang, X. Rui and Y. Yu, *Small Methods*, 2025, 2402220.

31. C. Li and Y. Du, *ACS Nano*, 2025, **19**, 4121-4155.

32. X. Li, J. Liang, X. Yang, K. R. Adair, C. Wang, F. Zhao and X. Sun, *Energy & Environmental Science*, 2020, **13**, 1429-1461.

33. D. C. Ginnings and T. E. Phipps, *Journal of the American Chemical Society*, 1930, **52**, 1340-1345.

34. T. Asano, A. Sakai, S. Ouchi, M. Sakaida, A. Miyazaki and S. Hasegawa, *Advanced Materials*, 2018, **30**, 1803075.

View Article Online
DOI: 10.1039/D5EB00064E

35. X. Li, J. Liang, N. Chen, J. Luo, K. R. Adair, C. Wang, M. N. Banis, T.-K. Sham, L. Zhang, S. Zhao, S. Lu, H. Huang, R. Li and X. Sun, *Angewandte Chemie International Edition*, 2019, **58**, 16427-16432.

36. K. Wang, Q. Ren, Z. Gu, C. Duan, J. Wang, F. Zhu, Y. Fu, J. Hao, J. Zhu, L. He, C.-W. Wang, Y. Lu, J. Ma and C. Ma, *Nature Communications*, 2021, **12**, 4410.

37. S. Zhang, F. Zhao, J. Chen, J. Fu, J. Luo, S. H. Alahakoon, L.-Y. Chang, R. Feng, M. Shakouri, J. Liang, Y. Zhao, X. Li, L. He, Y. Huang, T.-K. Sham and X. Sun, *Nature Communications*, 2023, **14**, 3780.

38. Y. Tanaka, K. Ueno, K. Mizuno, K. Takeuchi, T. Asano and A. Sakai, *Angewandte Chemie International Edition*, 2023, **62**, e202217581.

39. T. Dai, S. Wu, Y. Lu, Y. Yang, Y. Liu, C. Chang, X. Rong, R. Xiao, J. Zhao, Y. Liu, W. Wang, L. Chen and Y.-S. Hu, *Nature Energy*, 2023, **8**, 1221-1228.

40. H. Kwak, J. Lyoo, J. Park, Y. Han, R. Asakura, A. Remhof, C. Battaglia, H. Kim, S.-T. Hong and Y. S. Jung, *Energy Storage Materials*, 2021, **37**, 47-54.

41. Y. Hu, J. Fu, J. Xu, J. Luo, F. Zhao, H. Su, Y. Liu, X. Lin, W. Li, J. T. Kim, X. Hao, X. Yao, Y. Sun, J. Ma, H. Ren, M. Yang, Y. Huang and X. Sun, *Matter*, 2024, **7**, 1018-1034.

42. E. A. Wu, S. Banerjee, H. Tang, P. M. Richardson, J.-M. Doux, J. Qi, Z. Zhu, A. Grenier, Y. Li, E. Zhao, G. Deysher, E. Sebti, H. Nguyen, R. Stephens, G. Verbist, K. W. Chapman, R. J. Clément, A. Banerjee, Y. S. Meng and S. P. Ong, *Nature Communications*, 2021, **12**, 1256.

View Article Online
DOI: 10.1039/D5EB00064E

43. R. Schlem, A. Banik, M. Eckardt, M. Zobel and W. G. Zeier, *ACS Applied Energy Materials*, 2020, **3**, 10164-10173.

44. L. Zhou, J. D. Bazak, C. Li and L. F. Nazar, *ACS Energy Letters*, 2024, **9**, 4093-4101.

45. A. Bohnsack, G. Balzer, H.-U. Güdel, M. S. Wickleder and G. Meyer, *Zeitschrift für anorganische und allgemeine Chemie*, 1997, **623**, 1352-1356.

46. A. Bohnsack, F. Stenzel, A. Zajonc, G. Balzer, M. S. Wickleder and G. Meyer, *Zeitschrift für anorganische und allgemeine Chemie*, 1997, **623**, 1067-1073.

47. Y. Sun, G. Bian, W. Tao, C. Zhai, M. Zhong and Z. Qiao, *Calphad*, 2012, **39**, 1-10.

48. X. Meng, Y. Sun, S. Yuan, Z. Ma, Y. Wang and Z. Qiao, *Calphad*, 2006, **30**, 301-307.

49. P. Ridley, L. H. B. Nguyen, E. Sebti, B. Han, G. Duong, Y.-T. Chen, B. Sayahpour, A. Cronk, G. Deysher, S.-Y. Ham, J. A. S. Oh, E. A. Wu, D. H. S. Tan, J.-M. Doux, R. Clément, J. Jang and Y. S. Meng, *Matter*, 2024, **7**, 485-499.

50. S. Zhang, F. Zhao, L.-Y. Chang, Y.-C. Chuang, Z. Zhang, Y. Zhu, X. Hao, J. Fu, J. Chen, J. Luo, M. Li, Y. Gao, Y. Huang, T.-K. Sham, M. D. Gu, Y. Zhang, G. King and X. Sun, *Journal of the American Chemical Society*, 2024, **146**, 2977-2985.

51. S. Muy, J. Voss, R. Schlem, R. Koerver, S. J. Sedlmaier, F. Maglia, P. Lamp, W. G. Zeier and Y. Shao-Horn, *iScience*, 2019, **16**, 270-282.

52. C. Wang, J. Liang, J. Luo, J. Liu, X. Li, F. Zhao, R. Li, H. Huang, S. Zhao, L. Zhang, J. Wang and X. Sun, *Science Advances*, 2021, **7**, eabh1896.

53. Q. Wang, Y. Zhou, X. Wang, H. Guo, S. Gong, Z. Yao, F. Wu, J. Wang, S. Ganapathy, X. Bai, B. Li, C. Zhao, J. Janek and M. Wagemaker, *Nature Communications*, 2024, **15**, 1050.

View Article Online
DOI: 10.1039/D5EB00064E

54. P. Kuske, W. Schäfer and H. D. Lutz, *Materials Research Bulletin*, 1988, **23**, 1805-1808.

55. Z. Wei, L. F. Nazar and J. Janek, *Batteries & Supercaps*, 2024, **7**, e202400005.

56. H. D. Lutz, P. Kuske and K. Wussow, *Zeitschrift für anorganische und allgemeine Chemie*, 1987, **553**, 172-178.

57. M. Schneider, P. Kuske and H. D. Lutz, *Zeitschrift für Naturforschung B*, 1993, **48**, 1-6.

58. R. Kanno, Y. Takeda, K. Murata and O. Yamamoto, *Solid State Ionics*, 1990, **39**, 233-244.

59. X. Li, J. Liang, K. R. Adair, J. Li, W. Li, F. Zhao, Y. Hu, T.-K. Sham, L. Zhang, S. Zhao, S. Lu, H. Huang, R. Li, N. Chen and X. Sun, *Nano Letters*, 2020, **20**, 4384-4392.

60. J. Fu, S. Wang, J. Liang, S. H. Alahakoon, D. Wu, J. Luo, H. Duan, S. Zhang, F. Zhao, W. Li, M. Li, X. Hao, X. Li, J. Chen, N. Chen, G. King, L.-Y. Chang, R. Li, Y. Huang, M. Gu, T.-K. Sham, Y. Mo and X. Sun, *Journal of the American Chemical Society*, 2023, **145**, 2183-2194.

61. J. Liang, X. Li, S. Wang, K. R. Adair, W. Li, Y. Zhao, C. Wang, Y. Hu, L. Zhang, S. Zhao, S. Lu, H. Huang, R. Li, Y. Mo and X. Sun, *Journal of the American Chemical Society*, 2020, **142**, 7012-7022.

62. Z. Xu, X. Chen, K. Liu, R. Chen, X. Zeng and H. Zhu, *Chemistry of Materials*, 2019, **31**, 7425-7433.

63. R. Schlem, T. Bernges, C. Li, M. A. Kraft, N. Minafra and W. G. Zeier, *ACS Applied Energy Materials*, 2020, **3**, 3684-3691.

View Article Online
DOI: 10.1039/D5EB00064E

64. X. Li, J. T. Kim, J. Luo, C. Zhao, Y. Xu, T. Mei, R. Li, J. Liang and X. Sun, *Nature Communications*, 2024, **15**, 53.

65. F. Stenzel and G. Meyer, *Zeitschrift für anorganische und allgemeine Chemie*, 1993, **619**, 652-660.

66. H. D. Lutz, W. Schmidt and H. Haeuseler, *Journal of Physics and Chemistry of Solids*, 1981, **42**, 287-289.

67. R. Kanno, Y. Takeda, K. Takada and O. Yamamoto, *Journal of The Electrochemical Society*, 1984, **131**, 469.

68. C. J. J. Van Loon and J. De Jong, *Acta Crystallographica Section B*, 1975, **31**, 2549-2550.

69. L. Zhou, C. Y. Kwok, A. Shyamsunder, Q. Zhang, X. Wu and L. F. Nazar, *Energy & Environmental Science*, 2020, **13**, 2056-2063.

70. J. Liang, E. van der Maas, J. Luo, X. Li, N. Chen, K. R. Adair, W. Li, J. Li, Y. Hu, J. Liu, L. Zhang, S. Zhao, S. Lu, J. Wang, H. Huang, W. Zhao, S. Parnell, R. I. Smith, S. Ganapathy, M. Wagemaker and X. Sun, *Advanced Energy Materials*, 2022, **12**, 2103921.

71. Y.-C. Yin, J.-T. Yang, J.-D. Luo, G.-X. Lu, Z. Huang, J.-P. Wang, P. Li, F. Li, Y.-C. Wu, T. Tian, Y.-F. Meng, H.-S. Mo, Y.-H. Song, J.-N. Yang, L.-Z. Feng, T. Ma, W. Wen, K. Gong, L.-J. Wang, H.-X. Ju, Y. Xiao, Z. Li, X. Tao and H.-B. Yao, *Nature*, 2023, **616**, 77-83.

72. R. Schlem, S. Muy, N. Prinz, A. Banik, Y. Shao-Horn, M. Zobel and W. G. Zeier, *Advanced Energy Materials*, 2020, **10**, 1903719.

View Article Online
DOI: 10.1039/D5EB00064E

73. S. Y. Kim, K. Kaup, K.-H. Park, A. Assoud, L. Zhou, J. Liu, X. Wu and L. F. Nazar, *ACS Materials Letters*, 2021, **3**, 930-938.

74. K. Yamada, K. Kumano and T. Okuda, *Solid State Ionics*, 2005, **176**, 823-829.

75. S. Wang, Q. Bai, A. M. Nolan, Y. Liu, S. Gong, Q. Sun and Y. Mo, *Angewandte Chemie International Edition*, 2019, **58**, 8039-8043.

76. F. Lissner, K. Krämer, T. Schleid, G. Meyer, Z. Hu and G. Kaindl, *Zeitschrift für anorganische und allgemeine Chemie*, 1994, **620**, 444-450.

77. C. Fu, Y. Li, W. Xu, X. Feng, W. Gu, J. Liu, W. Deng, W. Wang, A. M. M. Abeykoon, L. Su, L. Zhu, X. Wu and H. Xiang, *Nature Communications*, 2024, **15**, 4315.

78. J. Fu, S. Wang, D. Wu, J. Luo, C. Wang, J. Liang, X. Lin, Y. Hu, S. Zhang, F. Zhao, W. Li, M. Li, H. Duan, Y. Zhao, M. Gu, T.-K. Sham, Y. Mo and X. Sun, *Advanced Materials*, 2024, **36**, 2308012.

79. F. Li, X. Cheng, G. Lu, Y.-C. Yin, Y.-C. Wu, R. Pan, J.-D. Luo, F. Huang, L.-Z. Feng, L.-L. Lu, T. Ma, L. Zheng, S. Jiao, R. Cao, Z.-P. Liu, H. Zhou, X. Tao, C. Shang and H.-B. Yao, *Journal of the American Chemical Society*, 2023, **145**, 27774-27787.

80. X. Lin, S. Zhang, M. Yang, B. Xiao, Y. Zhao, J. Luo, J. Fu, C. Wang, X. Li, W. Li, F. Yang, H. Duan, J. Liang, B. Fu, H. Abdolvand, J. Guo, G. King and X. Sun, *Nature Materials*, 2025, **24**, 83-91.

81. R. Xu, J. Yao, Z. Zhang, L. Li, Z. Wang, D. Song, X. Yan, C. Yu and L. Zhang, *Advanced Science*, 2022, **9**, 2204633.

82. S.-K. Jung, H. Gwon, G. Yoon, L. J. Miara, V. Lacivita and J.-S. Kim, *ACS Energy Letters*, 2021, **6**, 2006-2015.

View Article Online
DOI: 10.1039/D5EB00064E

83. S. V. Patel, V. Lacivita, H. Liu, E. Truong, Y. Jin, E. Wang, L. Miara, R. Kim, H. Gwon, R. Zhang, I. Hung, Z. Gan, S.-K. Jung and Y.-Y. Hu, *Science Advances*, **9**, eadj9930.

84. X. Yang, S. Gupta, Y. Chen, D. Sari, H.-M. Hau, Z. Cai, C. Dun, M. Qi, L. Ma, Y. Liu, J. J. Urban and G. Ceder, *Advanced Energy Materials*, 2024, **14**, 2400163.

85. K.-H. Park, K. Kaup, A. Assoud, Q. Zhang, X. Wu and L. F. Nazar, *ACS Energy Letters*, 2020, **5**, 533-539.

86. Y. Liu, S. Wang, A. M. Nolan, C. Ling and Y. Mo, *Advanced Energy Materials*, 2020, **10**, 2002356.

87. T. H. Wan and F. Ciucci, *ACS Applied Energy Materials*, 2021, **4**, 7930-7941.

88. L. Zhou, T.-T. Zuo, C. Y. Kwok, S. Y. Kim, A. Assoud, Q. Zhang, J. Janek and L. F. Nazar, *Nature Energy*, 2022, **7**, 83-93.

89. J. Wu, J. Li and X. Yao, *Advanced Functional Materials*, 2025, **35**, 2416671.

90. J. Park, D. Han, H. Kwak, Y. Han, Y. J. Choi, K.-W. Nam and Y. S. Jung, *Chemical Engineering Journal*, 2021, **425**, 130630.

91. H. Kwak, D. Han, J. P. Son, J. S. Kim, J. Park, K.-W. Nam, H. Kim and Y. S. Jung, *Chemical Engineering Journal*, 2022, **437**, 135413.

92. H. Kwak, D. Han, J. Lyoo, J. Park, S. H. Jung, Y. Han, G. Kwon, H. Kim, S.-T. Hong, K.-W. Nam and Y. S. Jung, *Advanced Energy Materials*, 2021, **11**, 2003190.

93. Y. Tomita, H. Matsushita, K. Kobayashi, Y. Maeda and K. Yamada, *Solid State Ionics*, 2008, **179**, 867-870.

94. Z. Liu, S. Ma, J. Liu, S. Xiong, Y. Ma and H. Chen, *ACS Energy Letters*, 2021, **6**, 298-304.

View Article Online
DOI: 10.1039/D5EB00064E

95. Z. Liu, P.-H. Chien, S. Wang, S. Song, M. Lu, S. Chen, S. Xia, J. Liu, Y. Mo and H. Chen, *Nature Chemistry*, 2024, **16**, 1584-1591.

96. M. A. Plass, S. Bette, R. E. Dinnebier and B. V. Lotsch, *Chemistry of Materials*, 2022, **34**, 3227-3235.

97. S. Yu, K. Kim, B. C. Wood, H.-G. Jung and K. Y. Chung, *Journal of Materials Chemistry A*, 2022, **10**, 24301-24309.

98. E. Umeshbabu, S. Maddukuri, Y. Hu, M. Fichtner and A. R. Munnangi, *ACS Applied Materials & Interfaces*, 2022, **14**, 25448-25456.

99. X. Luo, X. He, H. Su, Y. Zhong, X. Wang and J. Tu, *Chemical Engineering Journal*, 2023, **465**, 143036.

100. S. Zhang, F. Zhao, S. Wang, J. Liang, J. Wang, C. Wang, H. Zhang, K. Adair, W. Li, M. Li, H. Duan, Y. Zhao, R. Yu, R. Li, H. Huang, L. Zhang, S. Zhao, S. Lu, T.-K. Sham, Y. Mo and X. Sun, *Advanced Energy Materials*, 2021, **11**, 2100836.

101. H. Kwak, J.-S. Kim, D. Han, J. S. Kim, J. Park, G. Kwon, S.-M. Bak, U. Heo, C. Park, H.-W. Lee, K.-W. Nam, D.-H. Seo and Y. S. Jung, *Nature Communications*, 2023, **14**, 2459.

102. J. Wang, F. Chen, L. Hu and C. Ma, *Nano Letters*, 2023, **23**, 6081-6087.

103. B. Li, Y. Li, H.-S. Zhang, T.-T. Wu, S. Guo and A.-M. Cao, *Science China Materials*, 2023, **66**, 3123-3128.

104. K.-H. Park, S. Y. Kim, M. Jung, S.-B. Lee, M.-J. Kim, I.-J. Yang, J.-H. Hwang, W. Cho, G. Chen, K. Kim and J. Yu, *ACS Applied Materials & Interfaces*, 2023, **15**, 58367-58376.

View Article Online
DOI: 10.1039/D5EB00064E

105. B. Hong, L. Gao, C. Li, G. Lai, J. Zhu, D. Huang, Y. Zuo, W. Yin, M. Sun, S. Zhao, J. Zheng, S. Han and R. Zou, *Nature Communications*, 2025, **16**, 143.

106. B. Hong, L. Gao, P. Nan, Y. Li, M. Liu, R. Zou, J. Gu, Q. Xu, J. Zhu and S. Han, *Angewandte Chemie International Edition*, 2025, **64**, e202415847.

107. Z. Song, T. Wang, H. Yang, W. H. Kan, Y. Chen, Q. Yu, L. Wang, Y. Zhang, Y. Dai, H. Chen, W. Yin, T. Honda, M. Avdeev, H. Xu, J. Ma, Y. Huang and W. Luo, *Nature Communications*, 2024, **15**, 1481.

108. X. Sun, *Science Bulletin*, 2023, **68**, 2682-2683.

109. W. Wang, *Materials Futures*, 2023, **2**, 047502.

110. Y. Ren and C.-W. Nan, *Journal of Materiomics*, 2024, **10**, 707-708.

111. S. Zhang, Y. Xu, H. Wu, T. Pang, N. Zhang, C. Zhao, J. Yue, J. Fu, S. Xia, X. Zhu, G. Wang, H. Duan, B. Xiao, T. Mei, J. Liang, X. Sun and X. Li, *Angewandte Chemie International Edition*, 2024, **63**, e202401373.

112. G. Wang, S. Zhang, H. Wu, M. Zheng, C. Zhao, J. Liang, L. Zhou, J. Yue, X. Zhu, Y. Xu, N. Zhang, T. Pang, J. Fu, W. Li, Y. Xia, W. Yin, X. Sun and X. Li, *Advanced Materials*, 2025, **37**, 2410402.

113. H. Duan, C. Wang, X.-S. Zhang, J. Fu, W. Li, J. Wan, R. Yu, M. Fan, F. Ren, S. Wang, M. Zheng, X. Li, J. Liang, R. Wen, S. Xin, Y.-G. Guo and X. Sun, *Journal of the American Chemical Society*, 2024, **146**, 29335-29343.

114. I. You, B. Singh, M. Cui, G. Goward, L. Qian, Z. Arthur, G. King and L. F. Nazar, *Energy & Environmental Science*, 2025, **18**, 478-491.

View Article Online
DOI: 10.1039/D5EB00064E

115. L. Shen, J.-L. Li, W.-J. Kong, C.-X. Bi, P. Xu, X.-Y. Huang, W.-Z. Huang, F. Fu, Y.-C. Le, C.-Z. Zhao, H. Yuan, J.-Q. Huang and Q. Zhang, *Advanced Functional Materials*, 2024, **34**, 2408571.

116. X. Lin, Y. Zhao, C. Wang, J. Luo, J. Fu, B. Xiao, Y. Gao, W. Li, S. Zhang, J. Xu, F. Yang, X. Hao, H. Duan, Y. Sun, J. Guo, Y. Huang and X. Sun, *Angewandte Chemie International Edition*, 2024, **63**, e202314181.

117. D. Li, D. Yu, G. Zhang, A. Du, Z. Ye, Y. Jia, W. Hou, T. Xu, F. Li, S. Chi, Y. Zhu and C. Yang, *Angewandte Chemie International Edition*, 2025, **64**, e202419735.

118. W. Li, J. Liang, M. Li, K. R. Adair, X. Li, Y. Hu, Q. Xiao, R. Feng, R. Li, L. Zhang, S. Lu, H. Huang, S. Zhao, T.-K. Sham and X. Sun, *Chemistry of Materials*, 2020, **32**, 7019-7027.

119. Y. Zhu and Y. Mo, *Angewandte Chemie International Edition*, 2020, **59**, 17472-17476.

120. S. Wang, X. Xu, C. Cui, C. Zeng, J. Liang, J. Fu, R. Zhang, T. Zhai and H. Li, *Advanced Functional Materials*, 2022, **32**, 2108805.

121. R. L. Sacci, T. H. Bennett, A. R. Drews, V. Anandan, M. J. Kirkham, L. L. Daemen and J. Nanda, *Journal of Materials Chemistry A*, 2021, **9**, 990-996.

122. Y. Qie, S. Wang, S. Fu, H. Xie, Q. Sun and P. Jena, *The Journal of Physical Chemistry Letters*, 2020, **11**, 3376-3383.

123. G. H. Chun, J. H. Shim and S. Yu, *ACS Applied Materials & Interfaces*, 2022, **14**, 1241-1248.

124. S. Wenzel, T. Leichtweiss, D. Krüger, J. Sann and J. Janek, *Solid State Ionics*, 2015, **278**, 98-105.

View Article Online
DOI: 10.1039/D5EB00064E

125. D. Park, H. Park, Y. Lee, S.-O. Kim, H.-G. Jung, K. Y. Chung, J. H. Shim and S. Yu, *ACS Applied Materials & Interfaces*, 2020, **12**, 34806-34814.

126. G. Xu, L. Luo, J. Liang, S. Zhao, R. Yang, C. Wang, T. Yu, L. Wang, W. Xiao, J. Wang, J. Yu and X. Sun, *Nano Energy*, 2022, **92**, 106674.

127. Y. Han, S. H. Jung, H. Kwak, S. Jun, H. H. Kwak, J. H. Lee, S.-T. Hong and Y. S. Jung, *Advanced Energy Materials*, 2021, **11**, 2100126.

128. S. H. Jung, U.-H. Kim, J.-H. Kim, S. Jun, C. S. Yoon, Y. S. Jung and Y.-K. Sun, *Advanced Energy Materials*, 2020, **10**, 1903360.

129. F. Zhao, S. Zhang, S. Wang, C. M. Andrei, H. Yuan, J. Zhou, J. Wang, Z. Zhuo, Y. Zhong, H. Su, J. T. Kim, R. Yu, Y. Gao, J. Guo, T.-K. Sham, Y. Mo and X. Sun, *Energy & Environmental Science*, 2024, **17**, 4055-4063.

130. Y. Fu and C. Ma, *Science China Materials*, 2021, **64**, 1378-1385.

131. L. M. Riegger, R. Schlem, J. Sann, W. G. Zeier and J. Janek, *Angewandte Chemie International Edition*, 2021, **60**, 6718-6723.

132. W. Li, M. Li, S. Wang, P.-H. Chien, J. Luo, J. Fu, X. Lin, G. King, R. Feng, J. Wang, J. Zhou, R. Li, J. Liu, Y. Mo, T.-K. Sham and X. Sun, *Nature Nanotechnology*, 2025, **20**, 265-275.

133. W. Li, M. Li, P.-H. Chien, S. Wang, C. Yu, G. King, Y. Hu, Q. Xiao, M. Shakouri, R. Feng, B. Fu, H. Abdolvand, A. Fraser, R. Li, Y. Huang, J. Liu, Y. Mo, T.-K. Sham and X. Sun, *Science Advances*, **9**, eadh4626.

134. B. Ma, R. Li, H. Zhu, T. Zhou, L. Lv, H. Zhang, S. Zhang, L. Chen, J. Wang, X. Xiao, T. Deng, L. Chen, C. Wang and X. Fan, *Advanced Materials*, 2024, **36**, 2402324.

View Article Online
DOI: 10.1039/D5EB00064E

135. S. Zhang, F. Zhao, H. Su, Y. Zhong, J. Liang, J. Chen, M. L. Zheng, J. Liu, L.-Y. Chang, J. Fu, S. H. Alahakoon, Y. Hu, Y. Liu, Y. Huang, J. Tu, T.-K. Sham and X. Sun, *Angewandte Chemie International Edition*, 2024, **63**, e202316360.

136. H. Zhang, F. Xu, X. Chen and W. Xia, *Journal*, 2023, **9**.

137. H. Wu, J. Qu, X. Yan, S. Zhang, X. Wang, J. Liang, N. Zhang, B. Dai, J. Yue, T. Pang, T. Mei, Y. Luo, H. Lai, X. Wang, L. Zhou, S. Wang, X. Sun and X. Li, *Advanced Materials*, 2025, **n/a**, 2502067.

138. Y. Li, Q. Liu, S. Wu, L. Geng, J. Popovic, Y. Li, Z. Chen, H. Wang, Y. Wang and T. Dai, *Journal of the American Chemical Society*, 2023, **145**, 10576-10583.

139. Z. Li, Y. Mu, K. Lü, G. Kang, T. Yang, S. Huang, M. Wei, L. Zeng and Y. Li, *Angewandte Chemie International Edition*, 2025, **64**, e202501749.

140. Y. Wu, L. Wang, S. Wei, X. Bi, H. Zhuo, W. Xiao, T. Yu, Y. Duan, C. Zhao, R. Yang, J. Liang, X. Li, J. Wang and X. Sun, *Advanced Energy Materials*, 2024, **14**, 2401528.

141. L. Zhou, S. Zhang, W. Li, B. Li, N. S. Grundish, P. Ren, X. Wang, N. Wu, W. Zhou and Y. Li, *Journal of the American Chemical Society*, 2025, **147**, 15136-15145.

Data availability statements

View Article Online
DOI: 10.1039/D5EB00064E

No primary research results, software or code have been included and no new data were generated or analysed as part of this review.